

Isothermal transport of a near-critical binary fluid mixture through a capillary tube with the preferential adsorption

Shunsuke Yabunaka*

*Advanced Science Research Center,
Japan Atomic Energy Agency, Tokai, 319-1195, Japan*

Youhei Fujitani†

*School of Fundamental Science and Technology,
Keio University, Yokohama 223-8522, Japan*

(Dated: May 17, 2022)

Abstract

We study isothermal transport of a binary fluid mixture, which lies in the homogeneous phase near the demixing critical point, through a capillary tube. A short-range interaction is assumed between each mixture component and tube's wall surface, which usually attracts one component more than the other. The resulting preferential adsorption becomes significant owing to large osmotic susceptibility. The mixture flowing out of the tube is rich in the preferred component when flow is driven by the pressure difference between the reservoirs. When flow is driven by the mass-fraction difference, the total mass flow occurs in the presence of the preferential adsorption. These phenomena can be regarded as cross effects linked by the reciprocal relation. The latter implies that diffusioosmosis arises from the free energy of the bulk of the mixture not involving the surface potential, unlike usual diffusioosmosis far from the critical point. We also study these phenomena numerically by using the hydrodynamics based on the coarse-grained free-energy functional, which was previously obtained to reveal near-critical static properties, and using material constants, which were previously obtained in some experimental studies. Influence of the critical enhancement of the transport coefficients is found to be negligible because of off-critical composition in the tube. It is also shown that the conductance, or the total mass flow rate under a given mass-fraction difference, can change non-monotonically with the temperature. The change is well expected to be large enough to be detected experimentally.

PACS numbers:

*Electronic address: yabunaka123@gmail.com

†Electronic address: youhei@appi.keio.ac.jp

I. INTRODUCTION

In this article, a binary fluid mixture containing no ions and lying in the homogeneous phase close to the demixing critical point is considered, and is simply referred to as a mixture. A short-range interaction, such as a dipole-dipole interaction, is assumed between each mixture component and a solid surface in contact with a mixture. Usually, one component is more attracted by the surface owing to difference in the interactions. The adsorption layer, where the preferred component is more concentrated, can be of significant thickness because of large osmotic susceptibility of a mixture [1–5]. Some static properties due to the preferential adsorption (PA) have been studied by using the renormalized local functional theory [11, 12]. At equilibrium, the composition profile significantly fluctuates on length scales smaller than the correlation length, which can reach 100 nm experimentally. After coarse-grained, many profiles that differ only on these scales are unified into much fewer profiles. In the theory, the free-energy functional, coarse-grained up to the local correlation length, is minimized by the equilibrium profile, which is made inhomogeneous by the PA.

We can apply hydrodynamics to study flow of a mixture if the flow has a typical length large enough in comparison to the correlation length [6, 7]. The hydrodynamics can be formulated from a coarse-grained free-energy functional [8]. The inhomogeneity of the composition profile, linked with that of the correlation length, yields additional hydrodynamic stress. The transport coefficients appearing in the hydrodynamics, enhanced by critical fluctuations [9, 10], are dependent on the local correlation length. Using the hydrodynamics based on the renormalized local functional theory [13, 14], the present authors calculated the drag coefficient of a colloidal particle in a mixture, which has the critical composition far from the particle [15]. The particle motion deforms the surrounding adsorption layer, which influences the drag force. The inhomogeneity of the correlation length was found to be crucial for its dependence on the temperature.

We consider isothermal transport of a mixture through a tube connecting two sufficiently large reservoirs. The transport is assumed to be caused by imposed differences in pressure and mass fraction between the reservoirs, with the mixture remaining in the homogeneous

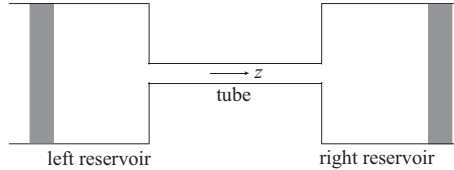


FIG. 1: Schematic of a situation supposed in our formulation. A mixture is filled in the container composed of two reservoirs and a tube connecting them. The tube extends along the z axis, with the right reservoir lying on the positive side. Thick walls represent pistons.

phase. One mixture component can be preferentially adsorbed by the tube wall. A supposed situation is schematically drawn in Fig. 1. A pressure difference is imposed by manipulating the pistons, whereas a mass-fraction difference is imposed by setting mixtures with different compositions in the reservoirs. Applying the hydrodynamics for a weak stationary laminar flow in the tube [16], we study how the PA onto the tube wall affects the transport properties. The tube is assumed to be so thin that the adsorption layer is not negligible but is so thick that the no-slip boundary condition can be imposed. The tube is assumed to be so long that effects of tube edges on the laminar flow and on the mixture in each reservoir are negligible. In particular, inhomogeneity of the correlation length is taken into account in our calculation, unlike in the previous studies on similar isothermal transports [17–19].

Much attention has been paid to osmotic flow of a solution through a channel [20–31]. A solution in the interfacial layer formed immediately near a channel wall can have distinct properties due to some interaction potential between a solute and a channel’s wall surface. In a nonelectrolyte solution, the layer can be generated by the van der Waals interaction or some dipole–dipole interaction. When a gradient of solute concentration is imposed in the channel direction, some force exerted on only the solution in the interfacial layer can yield an apparent slip velocity between the wall and the bulk of the solution, resulting in convection of the latter. This is the conventional explanation for diffusioosmosis [32, 33]. In contrast, as shown later, when the mass-fraction difference is imposed in our problem, diffusioosmosis arises via the anisotropic stress, which does not involve any potential due to the tube’s wall surface but originates from the free energy in the bulk of a mixture. The length range over which each component interacts with the surface is invisible in

our coarse-grained description. The anisotropic stress varies inside the adsorption layer distinctly thick in comparison with the molecular size. This mechanism is not considered in the conventional theory on diffusioosmosis, and was recently discussed as a possible mechanism for diffusiophoresis by one of the present authors [34]. The resulting mass flow rates should be sensitive to the temperature owing to the critical singularity of the susceptibility.

In Section II, we review the Onsager coefficients, formulate the hydrodynamics, and describe the calculation procedure. The pressure felt by the piston is equal to the negative of the grand-potential density in the central region of the reservoir; this density depends not only on the total mass density, denoted by ρ , but also on the composition. We need not assume the mixture to be incompressible in the dynamics. In Section III, we derive some results, neither using the renormalized local functional theory nor assuming that the total mass density is homogeneous at equilibrium. In Sections IIC and III, the cross-section perpendicular to a tube axis is assumed to be the same throughout the tube, which need not be cylindrical. We numerically calculate the Onsager coefficients and the mass flow rates by using a specified model based on the renormalized local functional theory. As mentioned in Section IV, it is assumed in this model that the tube is cylindrical, that ρ is homogeneous at equilibrium, and that the mixture at equilibrium has the critical composition in the central region of the reservoir. In the numerical results of Section V, we use material constants of a mixture of 2,6-lutidine and water and ones of a mixture of nitroethane and 3-methylpentane. The last section is devoted to a summary and further discussion.

II. FORMULATION

Mixture components are referred to as a and b; ρ_n denotes the mass density of the component n (= a or b). The total mass density ρ equals $\rho_a + \rho_b$, whereas the difference $\rho_a - \rho_b$ is denoted by φ . We write c_n for ρ_n/ρ and μ_n for the chemical potential conjugate to ρ_n . In the bulk of an equilibrium mixture, μ_n is a function of the temperature (denoted by T), pressure (P), and the mass fraction of the component a (c_a). We write μ_{\pm} for $(\mu_a \pm \mu_b)/2$, and define μ as the deviation of μ_- from its critical value, $(\mu_-)_c$. The subscript c generally indicates the value at the critical point; ρ and φ are conjugate to μ_+ and μ_- , respectively.

A quantity in each reservoir is indicated with the subscript R or L ; \mathcal{M}_{nR} denotes the total mass of the component n in the right reservoir of Fig. 1.

A. Thermodynamics

We first consider entropy fluctuations of an equilibrium mixture in the isolated container with the pistons fixed (Fig. 1). Neglecting the contribution from the mixture in the tube, we can regard the total entropy of the mixture in the container, denoted by S , as a function of \mathcal{M}_{aR} , \mathcal{M}_{bR} , and the internal energy of the mixture in the right reservoir, because the total mass of each component and the total internal energy in the isolated container are constant. Writing t for the time, we have

$$\frac{dS}{dt} = \sum_{n=a,b} \frac{\partial S}{\partial \mathcal{M}_{nR}} \frac{d\mathcal{M}_{nR}}{dt} = - \sum_{n=a,b} \frac{\mu_{nR} - \mu_{nL}}{T} \frac{d\mathcal{M}_{nR}}{dt} \quad (1)$$

up to the second order of the magnitudes of the deviations. Here, we drop the term involving the internal energy, which vanishes on the isothermal condition. Equation (1) is included in Eq. (XV-55) of Ref. [16], and tells that the thermodynamic forces are given by $-(\mu_{nR} - \mu_{nL})/T$ and the conjugate fluxes by $d\mathcal{M}_{nR}/(dt)$, with n being a and b, in the isothermal transport.

Imposing weak thermodynamic forces on an equilibrium state throughout the mixture, we consider a weak flow in terms of the linear nonequilibrium thermodynamics. The mass densities are homogeneous in the central region of each reservoir; a superscript (ref) is added to a quantity in this region in the equilibrium state. For example, the value of c_n shared by the central regions in the reservoirs in the equilibrium state is referred to as $c_n^{(\text{ref})}$, which is here assumed to be either equal or close to the value at the critical composition, c_{nc} . A flow is driven by a nonzero value of δc_a , which is defined as the difference of the value of c_a in the central region of the left reservoir subtracted from that of the right reservoir. In this manner, δ is used to indicate the difference in a quantity between these regions. An equilibrium mixture has homogeneous chemical potentials. Even in the presence of flow in the tube, the mixture is considered to be at equilibrium in the large reservoirs. The difference in the numerator in Eq. (1) can be written as $\delta\mu_n$. In each reservoir, because of the mechanical balance, the pressure felt by the right (left) piston in Fig. 1 is always the same as the

pressure in the central region of the right (left) reservoir. As a result, δP equals the difference between the pressures felt by the pistons on both sides and can be controlled externally.

We consider another set of forces, $-\delta P/T$ and $-\delta\mu/T$. Neglecting possible effects of the tube edges, we assume that P and μ are constant on the cross section at each tube edge to regard δP and $\delta\mu$ as the respective differences between the tube edges. With the aid of the Gibbs-Duhem relation for $\delta T = 0$, we have

$$\begin{pmatrix} \delta P \\ \delta\mu \end{pmatrix} = \begin{pmatrix} \rho_a^{(\text{ref})} & \rho_b^{(\text{ref})} \\ 1/2 & -1/2 \end{pmatrix} \begin{pmatrix} \delta\mu_a \\ \delta\mu_b \end{pmatrix}. \quad (2)$$

Using the coefficient matrix above, denoted by Θ , we convert the fluxes in Eq. (1) to the fluxes conjugate to $(-\delta P/T, -\delta\mu/T)$. The fluxes, $(\mathcal{I}, \mathcal{J})$, are defined by the first equality of

$$[\Theta^{-1}]^T \begin{pmatrix} d\mathcal{M}_{\text{aR}}/(dt) \\ d\mathcal{M}_{\text{bR}}/(dt) \end{pmatrix} = \begin{pmatrix} \mathcal{I} \\ \mathcal{J} \end{pmatrix} = \mathcal{L} \begin{pmatrix} -\delta P/T \\ -\delta\mu/T \end{pmatrix}, \quad (3)$$

where the superscript T indicates the transposition. The second equality above represents the linear phenomenological equations (LPEs) [35, 36]. The components of the coefficient matrix \mathcal{L} are Onsager coefficients, satisfying the reciprocal relation, $\mathcal{L}_{12} = \mathcal{L}_{21}$, with the matrix being positive semi-definite. Using the first equality of Eq. (3), we have

$$\frac{d}{dt}\mathcal{M}_{n\text{R}} = \rho_n^{(\text{ref})}\mathcal{I} \pm \frac{1}{2}\mathcal{J}, \quad (4)$$

where the upper (lower) sign is taken for $n = \text{a}$ (b) in the double sign. The total mass flow rate is denoted by $d\mathcal{M}_{\text{R}}/(dt)$ and equals the sum of Eq. (4) over $n = \text{a}$ and b , *i.e.*, $\rho^{(\text{ref})}\mathcal{I}$.

We later discuss flow driven by the pressure difference ($\delta P \neq 0, \delta c_a = 0$) and flow driven by the mass-fraction difference ($\delta P = 0, \delta c_a \neq 0$); δc_a would be easier to handle experimentally than $\delta\mu$. The partial volume per unit mass of the component n , denoted by \bar{v}_n , is defined as the partial derivative of the mixture volume with respect to the mass of the component n with T, P , and the mass of the other component held constant. We write \bar{v}_\pm for $(\bar{v}_a \pm \bar{v}_b)/2$. The volume and masses are extensive variables, which leads to

$$1 = \bar{v}_a\rho_a + \bar{v}_b\rho_b = \bar{v}_+\rho + \bar{v}_-\varphi \quad (5)$$

in the bulk of an equilibrium mixture. The composition can be represented by either c_a or $\varphi \equiv \rho(2c_a - 1)$. For the isothermal transport, we have

$$\delta\mu_n = \left. \frac{\partial\mu_n}{\partial P} \right)_{T, c_a} \delta P + \left. \frac{\partial\mu_n}{\partial c_a} \right)_{T, P} \delta c_a, \quad (6)$$

where the fixed variables in the partial differentiation are indicated in the subscript of a right parenthesis and the partial derivatives are evaluated at the central region of the reservoir in the equilibrium state. The first derivative on the right-hand side (RHS) above equals $\bar{v}_n^{(\text{ref})}$ owing to a Maxwell relation derived from the Gibbs free energy. Thus, we have

$$\delta\mu = \bar{v}_-^{(\text{ref})} \delta P + \left. \frac{\partial\mu}{\partial c_a} \right)_{T, P} \delta c_a. \quad (7)$$

The second term on the RHS above represents the part of $\delta\mu$ caused by δc_a and is below denoted by $(\delta\mu)_P$. The partial derivative in the second term is positive owing to the thermodynamic stability, is proportional to the inverse of the osmotic susceptibility, as shown in Eq. (34) below, and becomes closer to zero as the critical point is approached. Using Eq. (7), we can convert the thermodynamic forces to $(-\delta P/T, -(\delta\mu)_P/T)$.

B. Hydrodynamics

We assume the free energy of the bulk of a mixture to be given by the volume integral of a function of ρ_a, ρ_b and the quadratic form of their gradients over the mixture region, V_{tot} . To describe the PA, we add the area integral of a function of (ρ_a, ρ_b) , or (ρ, φ) , over the interface between the mixture and the container, ∂V_{tot} . With f_{bulk} and f_{surf} denoting these functions, respectively, the free-energy functional is given by

$$F[\rho_a, \rho_b] = \int_{V_{\text{tot}}} d\mathbf{r} f_{\text{bulk}}(\rho, \varphi, \nabla\rho, \nabla\varphi) + \int_{\partial V_{\text{tot}}} dA f_{\text{surf}}(\rho, \varphi), \quad (8)$$

where the mass densities depend on the position \mathbf{r} . The dependence of f_{bulk} on the gradients is assumed to be only via $|\nabla\rho|^2, |\nabla\varphi|^2$, and $(\nabla\rho) \cdot (\nabla\varphi)$. Because Eq. (8) is the Helmholtz free energy of a mixture with $\rho_a(\mathbf{r})$ and $\rho_b(\mathbf{r})$ being given, $\mu_n(\mathbf{r})$ is given by the functional derivative of $F[\rho_a, \rho_b]$ with respect to $\rho_n(\mathbf{r})$ in the bulk of a mixture, which leads to

$$\mu_+ = \frac{\partial f_{\text{bulk}}}{\partial \rho} - \nabla \cdot \left(\frac{\partial f_{\text{bulk}}}{\partial \nabla \rho} \right) \quad \text{and} \quad \mu_- = \frac{\partial f_{\text{bulk}}}{\partial \varphi} - \nabla \cdot \left(\frac{\partial f_{\text{bulk}}}{\partial \nabla \varphi} \right). \quad (9)$$

We can obtain the reversible part of the pressure tensor, Π_{rev} , by considering how the free energy is changed by a quasistatic deformation of a mixture. Its scalar part, P , equals the negative of the grand-potential density, *i.e.*,

$$P = -f_{\text{bulk}} + \rho_a \mu_a + \rho_b \mu_b = -f_{\text{bulk}} + \rho \mu_+ + \varphi \mu_- . \quad (10)$$

As shown in Appendix A, with $\mathbf{1}$ denoting the identity tensor of order two, we have

$$\Pi_{\text{rev}} = P \mathbf{1} + \frac{\partial f_{\text{bulk}}}{\partial (\nabla \rho)} (\nabla \rho) + \frac{\partial f_{\text{bulk}}}{\partial (\nabla \varphi)} (\nabla \varphi) , \quad (11)$$

which is a symmetric tensor. After some algebra, we obtain

$$\nabla \cdot \Pi_{\text{rev}} = \rho \nabla \mu_+ + \varphi \nabla \mu . \quad (12)$$

For quantities in the central regions of the reservoirs, we use Eqs. (9) and (10) to find

$$\delta P = \rho^{(\text{ref})} \delta \mu_+ + \varphi^{(\text{ref})} \delta \mu . \quad (13)$$

Thus, considering Eq. (7), $\delta \mu_+$ is determined by δP and δc_a .

The diffusion flux of the component n ($= a$ or b), denoted by \mathbf{j}_n , is defined so that the sum $\mathbf{j}_a + \mathbf{j}_b$ vanishes. We have

$$\frac{\partial \rho_n}{\partial t} = -\nabla \cdot (\rho_n \mathbf{v}) - \nabla \cdot \mathbf{j}_n \quad (14)$$

from the mass conservation. The sum of the above over $n = a$ and b is

$$\frac{\partial \rho}{\partial t} = -\nabla \cdot (\rho \mathbf{v}) , \quad (15)$$

whereas the difference gives

$$\frac{\partial \varphi}{\partial t} = -\nabla \cdot (\varphi \mathbf{v}) - \nabla \cdot \mathbf{j} , \quad (16)$$

where \mathbf{j} is defined as $\mathbf{j}_a - \mathbf{j}_b$. The left-hand sides (LHSs) of Eqs. (14) – (16) vanish in the stationary state. We can assume \mathbf{j} to be equal to $-\Lambda \nabla \mu$, where Λ denotes the transport coefficient of the interdiffusion. The container's wall surface is assumed to be impermeable to the mixture, which means that the normal component of $\nabla \mu$ vanishes at ∂V_{tot} . As mentioned later, in a weak stationary laminar flow in the tube, $\nabla \cdot \mathbf{v}$ vanishes although ρ is not assumed to be constant. There, the momentum conservation gives

$$0 = -\rho \nabla \mu_+ - \varphi \nabla \mu + 2 \nabla \cdot (\eta_s E) , \quad (17)$$

where η_s is the shear viscosity and E is the rate-of-strain tensor. The no-slip boundary condition is imposed at ∂V_{tot} . The transport coefficients, η_s and Λ , can be inhomogeneous.

Because the fields are coarse-grained up to the local correlation length, the mass densities at equilibrium minimize the grand potential of a mixture, *i.e.*,

$$F[\rho_a, \rho_b] - \int_{V_{\text{tot}}} d\mathbf{r} \left[\mu_+^{(\text{ref})} \rho(\mathbf{r}) + \mu_-^{(\text{ref})} \varphi(\mathbf{r}) \right]. \quad (18)$$

Thus, the equilibrium mass densities satisfy the two equations in Eq. (9) with the superscript ^(ref) added to the chemical potentials, together with the boundary conditions

$$\mathbf{n}_{\partial V_{\text{tot}}} \cdot \frac{\partial f_{\text{bulk}}}{\partial(\nabla\rho)} + \frac{\partial f_{\text{surf}}}{\partial\rho} = \mathbf{n}_{\partial V_{\text{tot}}} \cdot \frac{\partial f_{\text{bulk}}}{\partial(\nabla\varphi)} + \frac{\partial f_{\text{surf}}}{\partial\varphi} = 0 \quad \text{at } \partial V_{\text{tot}}, \quad (19)$$

where $\mathbf{n}_{\partial V_{\text{tot}}}$ denotes the outward facing unit vector normal to ∂V_{tot} . Homogeneous chemical potentials imply the mechanical balance at equilibrium, $\nabla \cdot \Pi_{\text{rev}} = 0$, because of Eq. (12). Equation (5) need not hold in a region with inhomogeneous mass densities.

C. Perturbation scheme

Assuming that δP and δc_a are proportional to a dimensionless smallness parameter, ε , we calculate the fields in the tube up to the order of ε to obtain the Onsager coefficients. The superscripts ⁽⁰⁾ and ⁽¹⁾ are used to indicate the order of ε . For example, we have $\mu_{\pm} = \mu_{\pm}^{(0)} + \varepsilon \mu_{\pm}^{(1)}$ up to the order of ε , where $\mu_{\pm}^{(0)}$ respectively equal $\mu_{\pm}^{(\text{ref})}$. The tube is assumed to have the same cross section along the z axis with the right reservoir lying on the positive side (Fig. 1). Taking the Cartesian coordinates (x, y, z) , we can assume $\rho^{(0)}$ and $\varphi^{(0)}$ to be functions of x and y , which are coordinates on a cross section. Using the area integral over a cross section of the tube, S_{tube} , we have

$$\frac{d}{dt} \mathcal{M}_{nR} = \varepsilon \int_{S_{\text{tube}}} dA \left(\rho_n^{(0)} v_z^{(1)} + j_{nz}^{(1)} \right) \quad (20)$$

up to the order of ε . With the aid of the first equality of Eq. (3), Eq. (20) gives

$$\mathcal{I} = \frac{\varepsilon}{\rho^{(\text{ref})}} \int_{S_{\text{tube}}} dA \rho^{(0)} v_z^{(1)} \quad (21)$$

$$\text{and } \mathcal{J} = \varepsilon \int_{S_{\text{tube}}} dA \left[\left(\varphi^{(0)} - \frac{\rho^{(0)} \varphi^{(\text{ref})}}{\rho^{(\text{ref})}} \right) v_z^{(1)} + j_z^{(1)} \right]. \quad (22)$$

The transport coefficients η_s and Λ can be regarded as dependent on $\rho^{(0)}$ and $\varphi^{(0)}$ in the equations up to the order of ε . The resulting (x, y) -dependent coefficients are denoted by $\eta_0(x, y)$ and $\Lambda_0(x, y)$, respectively. In the absence of PA, the mass densities become homogeneous and Eq. (17) becomes the usual Stokes equation, $0 = -\nabla P + \eta_s \Delta \mathbf{v}$. In Appendix B, our formulation up to here is shown to be consistent with the reciprocal relation.

III. IMMEDIATE RESULTS FROM THE FORMULATION

Because \mathbf{v} vanishes for $\varepsilon = 0$, Eq. (15) in a stationary laminar flow in the tube gives

$$0 = \nabla \cdot \mathbf{v}^{(1)} = \partial_z v_z^{(1)}, \quad (23)$$

where ∂_z denotes the partial derivative with respect to z . We obtain

$$0 = \rho^{(0)} \bar{\nabla} \mu_+^{(1)} + \varphi^{(0)} \bar{\nabla} \mu^{(1)} \quad (24)$$

from the x and y components of Eq. (17). Here, $\bar{\nabla}$ represents the two-dimensional nabla defined on the (x, y) plane. The z component gives

$$\bar{\nabla} \cdot (\eta_0 \bar{\nabla} v_z^{(1)}) = \rho^{(0)} \partial_z \mu_+^{(1)} + \varphi^{(0)} \partial_z \mu^{(1)}, \quad (25)$$

where $v_z^{(1)}$ is regarded as a scalar on the plane. The LHS above is independent of z because of Eq. (23). In a stationary laminar flow, Eq. (16) yields $0 = \nabla \cdot (\Lambda_0 \nabla \mu^{(1)})$, *i.e.*,

$$0 = \bar{\nabla} \cdot (\Lambda_0 \bar{\nabla} \mu^{(1)}) + \Lambda_0 \partial_z^2 \mu^{(1)}. \quad (26)$$

The boundary condition of $\bar{\nabla} \mu^{(1)}$ on a cross section is given below Eq. (16). As assumed in the third paragraph of Section II A, μ is constant over the cross section at each of the tube edges. These conditions and Eq. (26) are satisfied when $\mu^{(1)}$ is a linear function of z and is independent of x and y . Then, because of Eqs. (24) and (25), $\mu_+^{(1)}$ is also a linear function of z and is independent of x and y . Hence, with the aid of Eq. (13), we obtain

$$\varepsilon \partial_z \mu_+^{(1)} = \frac{\delta P - \varphi^{(\text{ref})} \delta \mu}{\rho^{(\text{ref})} L_{\text{tube}}} \quad \text{and} \quad \varepsilon \partial_z \mu^{(1)} = \frac{\delta \mu}{L_{\text{tube}}}, \quad (27)$$

where L_{tube} denotes the length of the tube. Thus, Eq. (25) becomes

$$\varepsilon \bar{\nabla} \cdot (\eta_0 \bar{\nabla} v_z^{(1)}) = \frac{\rho^{(0)} \delta P}{\rho^{(\text{ref})} L_{\text{tube}}} + \left(\varphi^{(0)} - \frac{\rho^{(0)} \varphi^{(\text{ref})}}{\rho^{(\text{ref})}} \right) \frac{\delta \mu}{L_{\text{tube}}}. \quad (28)$$

Owing to $\mathbf{j}^{(1)} = -\Lambda_0 \nabla \mu^{(1)}$, $\mathbf{j}^{(1)}$, and hence $\mathbf{j}_a^{(1)} = -\mathbf{j}_b^{(1)}$, are along the z axis. This yields

$$\varepsilon j_z^{(1)}(x, y) = -\Lambda_0(x, y) \frac{\delta \mu}{L_{\text{tube}}} . \quad (29)$$

In the absence of PA, the difference in the parentheses on the RHS of Eq. (28) identically vanishes, and $v_z^{(1)}$ is independent of $\delta \mu$. That the difference identically vanishes is equivalent with that $c_a^{(0)}(x, y)$ equals $c_a^{(\text{ref})}$ for any (x, y) . This equality should mean no PA, and hence we can assume that the difference identically vanishes only in the absence of PA.

In the presence of PA, because $v_z^{(1)}$ satisfies Eq. (28) and the no-slip boundary condition at the tube wall, the solution for $v_z^{(1)}$ is the sum of a term proportional to δP and a term proportional to $\delta \mu$. Substituting this solution and Eq. (29) into Eqs. (21) and (22), we should be able to express the Onsager coefficients \mathcal{L}_{ij} , appearing in the LPEs of Eq. (3), in terms of the quantities at the order of ε^0 . Although the solution is not obtained at this stage, we find that \mathcal{L}_{11} and $\mathcal{L}_{12} = \mathcal{L}_{21}$ involve $v_z^{(1)}$, *i.e.*, convection. Part of the first term in the brackets of Eq. (22) contributes to \mathcal{L}_{22} and the second term also contributes to \mathcal{L}_{22} . We refer to the parts of \mathcal{L}_{22} produced by these contributions as \mathcal{L}_{22v} and \mathcal{L}_{22d} , respectively. The former involves convection, whereas the latter interdiffusion. Neither of them contributes to the total mass flow. Notably, $\rho^{(1)}$ and $\varphi^{(1)}$ can be determined by Eq. (9) once $\mu_{\pm}^{(1)}$ are given, but we need not know $\rho^{(1)}$ and $\varphi^{(1)}$ in calculating \mathcal{L}_{ij} .

In the absence of PA, because $\mathcal{L}_{12} = \mathcal{L}_{21}$ and \mathcal{L}_{22v} are found to vanish, the first term on the RHS of Eq. (4) is equal to $-\rho_n^{(\text{ref})} \mathcal{L}_{11} \delta P / T$ involving the convection, whereas the second term to $\mp \mathcal{L}_{22d} \delta \mu / (2T)$ involving the interdiffusion. This means that, when flow is driven by the pressure difference, *i.e.*, by $\delta P \neq 0$ and $\delta c_a = 0$, the convected part of a mixture has the mass fraction of $c_n^{(\text{ref})}$. Then, unless $\bar{v}_-^{(\text{ref})}$ vanishes in Eq. (7), the interdiffusion occurs in addition. In the absence, only the interdiffusion occurs and the total mass flow rate disappears when flow is driven by the mass-fraction difference, *i.e.*, by $\delta c_a \neq 0$ and $\delta P = 0$.

In the presence of PA, $-\rho_n^{(\text{ref})} \mathcal{L}_{12} \delta \mu / T$ emerges in the first term on the RHS of Eq. (4), whereas $\mp \mathcal{L}_{21} \delta P / (2T)$ and $\mp \mathcal{L}_{22v} \delta \mu / (2T)$ emerge in the second term. Because of the second of these three emergent terms, when flow is driven by the pressure difference, even the convected part of a mixture does not have the mass fraction of $c_n^{(\text{ref})}$, which is realized con-

sidering that the preferred component is concentrated in the tube. Because of the first and third of the emergent terms, not only the interdiffusion but also the convective transport occurs when flow is driven by the mass-fraction difference. In particular, the first term, involving \mathcal{L}_{12} , generates the total mass flow, which represents diffusioosmosis. The coefficients \mathcal{L}_{21} and \mathcal{L}_{12} represent the cross effects in the LPEs of Eq. (3).

IV. ELEMENTS FOR NUMERICAL CALCULATIONS

Below, we assume that a mixture, at equilibrium throughout, has the critical composition in the central region of the reservoir. In other words, we assume $\rho_n^{(\text{ref})} = \rho_{nc}$, which leads to $c_n^{(\text{ref})} = c_{nc}$, $\rho^{(\text{ref})} = \rho_c$, and $\varphi^{(\text{ref})} = \varphi_c$. The difference $\varphi(\mathbf{r}) - \varphi_c$, denoted by $\psi(\mathbf{r})$, is the order parameter of the phase separation. In the absence of PA ($h = 0$), $\psi(\mathbf{r})$ vanishes.

A. Free-energy functional

We assume that f_{bulk} is separated into the ρ -dependent part and ψ -dependent part. The former part is a function of ρ , denoted by $f_+(\rho)$, whereas the latter part consists of a function of ψ , denoted by $f_-(\psi)$, and the square gradient term. This term is written as $M_-(\psi) |\nabla\psi|^2 / 2$ with $M_-(\psi)$ denoting a positive function of ψ . The expressions of f_- and M_- are given in terms of the renormalized local functional theory [11, 12], as shown in the next subsection. In this theory, as mentioned in Appendix C, the functional is obtained by coarse-graining a bare model up to the local correlation length of composition fluctuations, and assuming $\varphi^{(\text{ref})} = \varphi_c$ amounts to assuming $\mu_-^{(0)} = (\mu_-)_c$, *i.e.*, $\mu^{(0)} = 0$. The correlation length is required to be much larger than a molecular size for the coarse-grained description to be valid. We also assume that f_{surf} , being independent of ρ , is proportional to ψ apart from an irrelevant constant. The negative of the constant of proportionality, denoted by h , is called the surface field [1, 37–39]. On these assumptions, Eq. (8) becomes

$$F[\rho_a, \rho_b] = \int_{V_{\text{tot}}} d\mathbf{r} \left[f_+(\rho) + f_-(\psi) + \frac{1}{2} M_-(\psi) |\nabla\psi|^2 \right] - h \int_{\partial V_{\text{tot}}} dA \psi. \quad (30)$$

Using the procedure mentioned in the last paragraph of Section II B, we can calculate $\rho^{(0)}$ and $\psi^{(0)}$. In particular, we find that $\rho^{(0)}$ is homogeneously equal to $\rho^{(\text{ref})} = \rho_c$. The equilibrium profile of the order parameter between the two parallel plates and the one around a

sphere are calculated using the renormalized local functional theory [11, 12, 15, 40, 41].

Because $\rho^{(0)}$ is homogeneous, Eq. (15) at the order of ε gives $\nabla \cdot \mathbf{v}^{(1)} = 0$ in a stationary flow, whether it is laminar or not. Equation (9) gives $\mu_+ = f'_+(\rho)$, which yields $\mu_+^{(1)} = \rho^{(1)} f''_+(\rho^{(0)})$. We define p as $\rho f'_+ - f_+$ to obtain $p^{(1)} = \rho^{(0)} \mu_+^{(1)}$, and Eq. (12) gives

$$\nabla \cdot \Pi_{\text{rev}}^{(1)} = \nabla p^{(1)} + \varphi^{(0)} \nabla \mu^{(1)} , \quad (31)$$

which is used in Ref. [15]. The first term on the RHS of Eq. (24) can be replaced by $\bar{\nabla} p^{(1)}$, whereas that of Eq. (25) by $\partial_z p^{(1)}$. In Eq. (21), \mathcal{I} becomes equal to the area integral of $\varepsilon v_z^{(1)}$ over S_{tube} and gives the flow rate. The difference in the parentheses of Eq. (22) equals $\psi^{(0)}$. Even if \mathcal{I} vanishes, the diffusion fluxes can change the composition of each reservoir, and hence its volume. Equations (10) and (13) give $P = p - f_- + \varphi \mu_-$ and

$$\delta P = \delta p + \varphi_c \delta \mu , \quad (32)$$

respectively. If the mass densities are homogeneous, we have

$$\left. \frac{\partial \mu}{\partial \varphi} \right)_{T\rho} = \left. \frac{\partial \mu}{\partial P} \right)_{Tc_a} \left. \frac{\partial P}{\partial \varphi} \right)_{T\rho} + \left. \frac{\partial \mu}{\partial c_a} \right)_{TP} \left. \frac{\partial c_a}{\partial \varphi} \right)_{T\rho} . \quad (33)$$

The LHS above equals the inverse of the osmotic susceptibility, $f''_-(\psi)$, whereas the first and second derivatives of the first term on the RHS equal \bar{v}_- and $f''_-(\psi)\varphi$, respectively. We can apply Eq. (5) and $\varphi \equiv \rho(2c_a - 1)$ for the second derivative of the second term. Thus, in the central region of the reservoir at equilibrium throughout the mixture, we obtain

$$\left. \frac{\partial \mu}{\partial c_a} \right)_{TP} = 2\rho_c^2 \bar{v}_+^{(\text{ref})} f''_-(0) , \quad (34)$$

which can be substituted into Eq. (7). As shown by Eq. (40) below, we have $f''_-(0) \propto \tau^\gamma$.

B. Non-dimensionalization

Using the conventional notation, we write β, γ, ν , and η for the critical exponents of binary mixtures near the demixing critical point. The exponent η represents the deviation from the straightforward dimensional analysis of the equal-time correlation function of the order-parameter fluctuations at the critical point. The critical temperature is denoted by T_c , and the reduced temperature τ is defined as $|T - T_c|/T_c$. In an equilibrium mixture with

the critical composition ($\psi = 0$), the correlation length, denoted by ξ , is given by $\xi_0\tau^{-\nu}$ in the critical regime, where ξ_0 is a material constant. In general, ξ depends on τ and ψ . The “distance” from the critical point is represented by ω , which is defined so that we have

$$\xi = \xi_0\omega^{-\nu} . \quad (35)$$

The values of the critical exponents are shown in Ref. [42]; we adopt $\nu = 0.630$ and $\eta = 0.0364$. The (hyper)scaling relations give $2\beta + \gamma = 3\nu$ and $\gamma = \nu(2 - \eta)$. Hereafter, the tube is assumed to be a cylinder with the radius r_{tube} . With r denoting the radial distance from the center axis, we can write $\psi^{(0)}(r)$, $\eta_0(r)$, and $\Lambda_0(r)$ because they are functions of r .

A dimensionless radial distance \hat{r} is defined as r/r_{tube} . A characteristic reduced temperature τ_* is defined so that ξ becomes r_{tube} for $\psi = 0$ at $\tau = \tau_*$. A characteristic order parameter ψ_* is defined so that ξ becomes r_{tube} for $\psi = \psi_*$ at $\tau = 0$. According to the self-consistent condition mentioned in Appendix C, these two definitions are equivalent to

$$\tau_* = \left(\frac{\xi_0}{r_{\text{tube}}} \right)^{1/\nu} \quad \text{and} \quad \psi_* = \frac{\tau_*^\beta}{\sqrt{C_2}} . \quad (36)$$

Here, C_2 is a material constant, whose estimates are obtained in Appendix C. We use $\hat{\tau} \equiv \tau/\tau_*$, $\hat{\omega} \equiv \omega/\tau_*$, and $\hat{\psi}^{(0)}(\hat{r}) \equiv \psi^{(0)}(r_{\text{tube}}\hat{r})/\psi_*$, and define μ_* as

$$\mu_* = \frac{k_{\text{B}}T_*}{3u^*r_{\text{tube}}^3\psi_*} , \quad (37)$$

where k_{B} , T_* , and u^* denote the Boltzmann constant, T at $\tau = \tau_*$, and the scaled coupling constant at the Wilson-Fisher fixed point. At the one loop order, u^* equals $2\pi^2/9$ in the three dimensions. Defining a dimensionless function \hat{f} as

$$\hat{f}(\hat{\psi}) = \hat{\omega}^{\gamma-1}\hat{\tau} \left(\frac{\hat{\psi}^2}{2} + \frac{\hat{\psi}^4}{12\hat{\omega}^{2\beta-1}\hat{\tau}} \right) , \quad (38)$$

we have $f_-(\psi) - (\mu_-)_c\varphi = \mu_*\psi_*T\hat{f}(\hat{\psi})/T_*$. The dependence of $\hat{\omega}$ on $\hat{\psi}$ and $\hat{\tau}$ is given by

$$\hat{\omega} = \hat{\tau} + \hat{\omega}^{1-2\beta}\hat{\psi}^2 , \quad (39)$$

which comes from the self-consistent condition mentioned in Appendix C. We find that $\hat{\omega}$ as a function of $\hat{\psi}$, and hence $\hat{f}(\hat{\psi})$, are even functions. We have $\hat{f}''(0) = \hat{\tau}^\gamma$ and

$$f_-''(0) = \frac{k_{\text{B}}TC_2\tau^\gamma}{3u^*\xi_0^3} . \quad (40)$$

Some profiles of $\hat{\psi}^{(0)}$ are shown in Fig. 10 (a) of Appendix D. We define dimensionless quantities $\delta\hat{P}$ and $\delta\hat{\mu}$ as $\delta P/(\mu_*\psi_*)$ and $\delta\mu/\mu_*$, respectively.

On length scales smaller than the correlation length, correlated clusters of the order parameter are randomly convected at equilibrium. On larger length scales, the transport coefficient for the interdiffusion Λ is enhanced because the convection is averaged out, and the viscosity η_s is also enhanced because the order parameter ψ and momentum density are dynamically coupled. The viscosity exhibits a weak singularity, and hence its nonuniversal background part is significant unless the mixture is very close to the critical point [43–46]. Later, we use experimental data for homogeneous compositions to obtain η_s as a function of τ and ψ . This function is used even when ψ is inhomogeneous. We introduce a dimensionless viscosity $\hat{\eta}(\hat{r}) \equiv \eta_0(r_{\text{tube}}\hat{r})/\eta_*$, where η_* is defined as the value of the singular part of η_s for $\tau = \tau_*$ and $\psi = 0$. The flow rate of Hagen-Poiseuille flow of a fluid, with the viscosity being η_* , driven by the pressure gradient $\mu_*\psi_*/L_{\text{tube}}$, is denoted by \mathcal{I}_* , which leads to

$$\mathcal{I}_* = \frac{\pi r_{\text{tube}}^4 \mu_* \psi_*}{8 \eta_* L_{\text{tube}}} = \frac{\pi k_B T_* r_{\text{tube}}}{24 u^* \eta_* L_{\text{tube}}}. \quad (41)$$

We define dimensionless quantities $\hat{\mathcal{I}}$ and $\hat{\mathcal{J}}$ as $\mathcal{I}/\mathcal{I}_*$ and $\mathcal{J}/(\psi_*\mathcal{I}_*)$, respectively.

We extend the previous theoretical result of $\Lambda(0)$ to obtain $\Lambda(\psi)$ for a homogeneous nonzero value of ψ , and then apply this extended result to a mixture with inhomogeneous composition, as discussed in Appendix E. Writing Λ_* for the value of Λ at $\psi = 0$ and $\tau = \tau_*$, we define a dimensionless coefficient $\hat{\Lambda}(\hat{r})$ as $T\Lambda_0(r_{\text{tube}}\hat{r})/(T_*\Lambda_*)$. Writing z_ψ for the dynamic critical exponent for the order-parameter fluctuations, we obtain

$$\hat{\Lambda}(\hat{r}) = \hat{\omega}^{\nu(z_\psi-2)} \left[\hat{f}''(\hat{\psi}^{(0)}(\hat{r})) \right]^{-1} \quad (42)$$

with the aid of $\hat{f}''(0) = 1$ at $\tau = \tau_*$. We use $z_\psi = 3.067$, as mentioned in Appendix E. Owing to Eq. (40), in the critical regime, $\hat{\Lambda}$ for $\psi = 0$ is enhanced with approximately the same power as ξ with respect to τ .

C. Formulas for the Onsager coefficients

In a cylindrical tube, we can write $v_z^{(1)}(r)$ and $j_z^{(1)}(r)$, and the LHS of Eq. (28) becomes $\varepsilon r^{-1} \partial_r \left(r \eta_0(r) \partial_r v_z^{(1)} \right)$. We have $v_z^{(1)} = 0$ at $r = r_{\text{tube}}$ because of the no-slip condition, and

$\partial_r v_z^{(1)} = 0$ at $r = 0$ because of the axisymmetry and smoothness of $v_z^{(1)}$. Thus, we obtain

$$\begin{aligned} \varepsilon v_z^{(1)}(r) = & -\frac{\delta P}{L_{\text{tube}}} \int_r^{r_{\text{tube}}} ds' \frac{1}{s' \eta_0(s')} \int_0^{s'} ds s \\ & -\frac{\delta \mu}{L_{\text{tube}}} \int_r^{r_{\text{tube}}} ds' \frac{1}{s' \eta_0(s')} \int_0^{s'} ds s \psi^{(0)}(s) . \end{aligned} \quad (43)$$

Substituting Eqs. (29) and (43) into Eqs. (21) and (22) yields formulas for \mathcal{L}_{ij} . For convenience, we define a dimensionless 2×2 matrix $\hat{\mathcal{L}}$ so that

$$\begin{pmatrix} \hat{\mathcal{I}} \\ \hat{\mathcal{J}} \end{pmatrix} = -\hat{\mathcal{L}} \begin{pmatrix} \delta \hat{P} \\ \delta \hat{\mu} \end{pmatrix} \quad (44)$$

holds, where $\delta \hat{P}$, $\delta \hat{\mu}$, $\hat{\mathcal{I}}$, and $\hat{\mathcal{J}}$ are defined in the preceding subsection. The components of $\hat{\mathcal{L}}$ are not strictly the Onsager coefficients because the column vectors on both the sides above are not conjugate fluxes and forces, although $\hat{\mathcal{L}}_{12}$ equals $\hat{\mathcal{L}}_{21}$. We have

$$\mathcal{L}_{11} = \frac{T\mathcal{I}_*}{\mu_* \psi_*} \hat{\mathcal{L}}_{11} , \quad \mathcal{L}_{12} = \frac{T\mathcal{I}_*}{\mu_*} \hat{\mathcal{L}}_{12} , \quad \text{and} \quad \mathcal{L}_{22} = \frac{T\mathcal{I}_* \psi_*}{\mu_*} \hat{\mathcal{L}}_{22} . \quad (45)$$

We define a functional Ω_1 as

$$\Omega_1[g] = 16 \int_0^1 dq_1 q_1 \hat{\psi}^{(0)}(q_1) \int_{q_1}^1 dq_2 \frac{1}{q_2 \hat{\eta}(q_2)} \int_0^{q_2} dq_3 q_3 g(q_3) , \quad (46)$$

and define another functional Ω_0 as the RHS above with $\hat{\psi}^{(0)}(q_1)$ being deleted. The formulas for \mathcal{L}_{ij} are given by Eq. (45) and

$$\begin{aligned} \hat{\mathcal{L}}_{11} = \Omega_0[1] , \quad \hat{\mathcal{L}}_{12} = \Omega_0[\hat{\psi}^{(0)}] , \quad \hat{\mathcal{L}}_{21} = \Omega_1[1] , \\ \text{and} \quad \hat{\mathcal{L}}_{22} = \Omega_1[\hat{\psi}^{(0)}] + \frac{16\pi}{9} \int_0^1 d\hat{r} \hat{r} \hat{\Lambda}(\hat{r}) . \end{aligned} \quad (47)$$

The coefficient $16\pi/9$ is derived in Appendix E. Thanks to this, we need not know the value of Λ_* in later calculations with dimensions. The terms \mathcal{L}_{22v} and \mathcal{L}_{22d} are non-dimensionalized to give the first and second terms on the RHS of the last entry in Eq. (47), which are denoted by $\hat{\mathcal{L}}_{22v}$ and $\hat{\mathcal{L}}_{22d}$, respectively. Only the latter term depends on $\hat{\Lambda}$ and involves the interdiffusion among all the terms on the RHSs in Eq. (47), whereas the others depend on $\hat{\eta}$ and involve convection. Interchanging the orders of the integrations, we have

$$\hat{\mathcal{L}}_{11} = 4 \int_0^1 dq \frac{q^3}{\hat{\eta}(q)} \quad \text{and} \quad \hat{\mathcal{L}}_{12} = \hat{\mathcal{L}}_{21} = 8 \int_0^1 dq_1 q_1 \hat{\psi}^{(0)}(q_1) \int_{q_1}^1 dq_2 \frac{q_2}{\hat{\eta}(q_2)} . \quad (48)$$

Dependence of $\hat{\mathcal{L}}_{11}$ on $\hat{\psi}^{(0)}$ is only via $\hat{\eta}$, and that of $\hat{\mathcal{L}}_{22d}$ is only via $\hat{\Lambda}$. In contrast, $\hat{\mathcal{L}}_{12} = \hat{\mathcal{L}}_{21}$ and $\hat{\mathcal{L}}_{22v}$ depend on $\hat{\psi}^{(0)}$ explicitly, and vanish if $\hat{\psi}^{(0)}$ vanishes, *i.e.*, if the PA is absent, as mentioned in the last paragraph of Section III. These explicit dependences can result from the difference in the parentheses in Eq. (22) and the same difference in Eq. (28). The integrand for $\hat{\mathcal{L}}_{12} = \hat{\mathcal{L}}_{21}$ in Eq. (48) contains $\hat{\psi}^{(0)}$ once because of either of the two origins, whereas the one for $\hat{\mathcal{L}}_{22v}$ in Eq. (47) twice because of both the origins. This suggests that $\hat{\mathcal{L}}_{22v}$ has a stronger dependence on $\hat{\psi}^{(0)}$.

When the pressure difference ($\delta P \neq 0$ and $\delta c_a = 0$) is imposed, the mass flow rates can be calculated by substituting the LPEs of Eq. (3) into Eq. (4) and using Eqs. (7) and (45), and hence $d\mathcal{M}_{nR}/(dt)$ equals δP multiplied by

$$-\frac{\mathcal{I}_* \rho_n^{(\text{ref})}}{\mu_* \psi_*} \left(\hat{\mathcal{L}}_{11} + \psi_* \bar{v}_-^{(\text{ref})} \hat{\mathcal{L}}_{12} \right) \mp \frac{\mathcal{I}_*}{2\mu_*} \left(\hat{\mathcal{L}}_{21} + \psi_* \bar{v}_-^{(\text{ref})} \hat{\mathcal{L}}_{22} \right) , \quad (49)$$

where the double sign implies the same as in Eq. (4). Notably, the interdiffusion is accompanied with the Hagen-Poiseuille flow in the absence of PA ($h = 0$) unless $\bar{v}_-^{(\text{ref})}$ vanishes. When the mass-fraction difference ($\delta P = 0$ and $\delta c_a \neq 0$) is imposed, $d\mathcal{M}_{nR}/(dt)$ equals $(\delta\mu)_P$ multiplied by

$$-\frac{\mathcal{I}_* \rho_n^{(\text{ref})}}{\mu_*} \hat{\mathcal{L}}_{12} \mp \frac{\mathcal{I}_* \psi_*}{2\mu_*} \hat{\mathcal{L}}_{22} . \quad (50)$$

V. NUMERICAL RESULTS

Our numerical results are obtained with the aid of the software Mathematica (Wolfram Research). The tube radius is put equal to $r_{\text{tube}} = 0.1 \mu\text{m}$. In Figs. 10 (b) and (c) of Appendix D, we show some flow profiles, which are consistent with our coarse-grained description. We abbreviate 2,6-lutidine and water to LW, and nitroethane and 3-methylpentane to NEMP.

A. Onsager coefficients for a mixture of LW

We consider a mixture of LW near the lower critical consolute point, taking 2,6-lutidine to be the component a. The value of $\xi_0 = 1.98 \times 10^{-1} \text{ nm}$ in Ref. [47] gives $\tau_* = 5.12 \times 10^{-5}$; we use $T_c = 307 \text{ K}$ and $c_{ac} = 0.290$. The estimate of C_2 in Appendix C

gives $\psi_* = 4.70 \times 10 \text{ kg/m}^3$, which leads to $\mu_* = 1.37 \times 10^{-2} \text{ m}^2/\text{s}^2$. In Appendix E, we obtain the viscosity as a function of the reduced temperature τ and the order parameter ψ and find $\eta_* = 2.44 \times 10^{-3} \text{ Pa}\cdot\text{s}$ by using the experimental data of Refs. [48, 49], part of which are replotted in Fig. 2(a). In this figure, the curves represent the function. Each of the black solid and green dashed curves appears to be composed of the background part of η_s alone, whereas a small peak due to the singular part appears on the red dash-dot curve. This curve has a nearly flat portion immediately to the right of the peak, which is clearly shown in the inset of Fig. 2(b). The background part is asymmetric about the vertical line at $c_a = c_{ac}$. In the homogeneous phase near the critical temperature, how ρ depends on c_a is measured in Ref. [50]. With the partial volumes, \bar{v}_a and \bar{v}_b , assumed to be constants, ρ is a function of c_a via Eq. (5). The curve-fit of the function to the data in Fig. 2(b) gives $\bar{v}_a = 1.03 \times 10^{-3} \text{ m}^3/\text{kg}$ and $\bar{v}_b = 1.00 \times 10^{-3} \text{ m}^3/\text{kg}$, which are respectively regarded as $\bar{v}_a^{(\text{ref})}$ and $\bar{v}_b^{(\text{ref})}$. These values yield $\rho_c = 9.88 \times 10^2 \text{ kg/m}^3$ and $\varphi_c = -4.15 \times 10^2 \text{ kg/m}^3$. In the following calculations, $|c_a - c_{ac}|$ in the tube at equilibrium is smaller than 0.15. According to the discussion in Section 6 of Ref. [15], the magnitude of the surface field h should be smaller than approximately $10 \text{ cm}^3/\text{s}^2$ when 2,6-lutidine adsorbs onto the solid surface.

Assuming $h = 0.1 \text{ cm}^3/\text{s}^2$, we use Eqs. (47) and (48) to obtain the results shown in Fig. 3(a), where $\hat{\mathcal{L}}_{12}$ is close to zero at $\tau = 6.4 \times 10^{-3}$ and increases eminently as τ decreases. Then, $\hat{\mathcal{L}}_{22}$ increases more eminently. From Fig. 3(b), we find that $\hat{\mathcal{L}}_{22v} = \hat{\mathcal{L}}_{22} - \hat{\mathcal{L}}_{22d}$ are close to zero at $\tau = 6.4 \times 10^{-3}$, and that the increase of $\hat{\mathcal{L}}_{22}$ with decreasing τ is mainly caused by that of \mathcal{L}_{22v} . These findings are expected from the statements in the penultimate paragraph of Section IV C; some plots of $\hat{\psi}^{(0)}$ are given in Fig. 10(a). In the absence of PA, noting that $\hat{\Lambda}$ becomes homogeneously equal to the value at the critical composition in Eq. (47), we calculate $\hat{\mathcal{L}}_{22d}$ and plot the results in Fig. 3(b). They show a significant increase with decreasing τ , which is caused by the critical enhancement of Λ . In the presence of PA, decrease in τ tends to cause the critical enhancement and tends to shift the composition away from the critical one (Fig. 10(a)). As a result of these conflicting tendencies, the values shown by the cross in Fig. 3(b) are approximately independent on τ .

When the sign of h is changed, that of $\hat{\psi}^{(0)}$ changes, as mentioned below Eq. (D1). This is reasonable because the changes can be made by renaming the components in the opposite

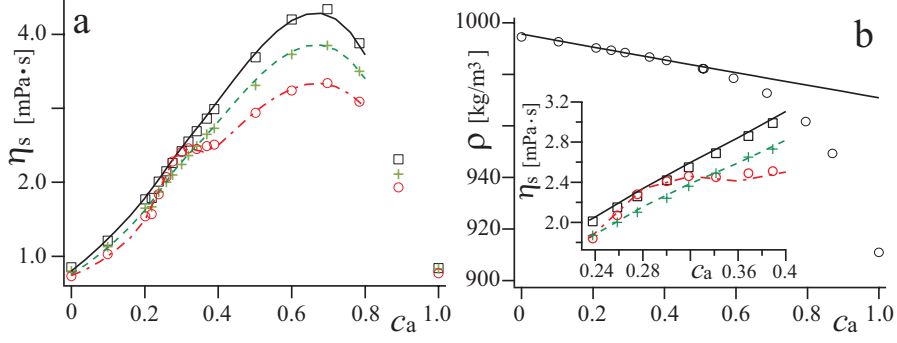


FIG. 2: Experimental data for a mixture of LW; c_a denotes the mass fraction of 2,6-lutidine. (a) Data of viscosity η_s at $\tau = 2.25 \times 10^{-2}$, 1.27×10^{-2} and 7.82×10^{-5} in Ref. [48] are replotted with the black square, green cross, and red circle, respectively. Curve fitting for $c_a < 0.8$ yield the black solid, green dashed, and red dash-dot curves for the respective values of τ . These values of τ are different from the values of τ used in the following figures of our numerical results for a mixture of LW. (b) The circle represents experimental data from Table III of Ref. [50] for the relationship between the total mass density ρ and the mass fraction c_a at 306.65 K. The solid curve is obtained by curve fitting to the data for $0.2 < c_a < 0.41$. The inset shows a magnified view of a part of (a).

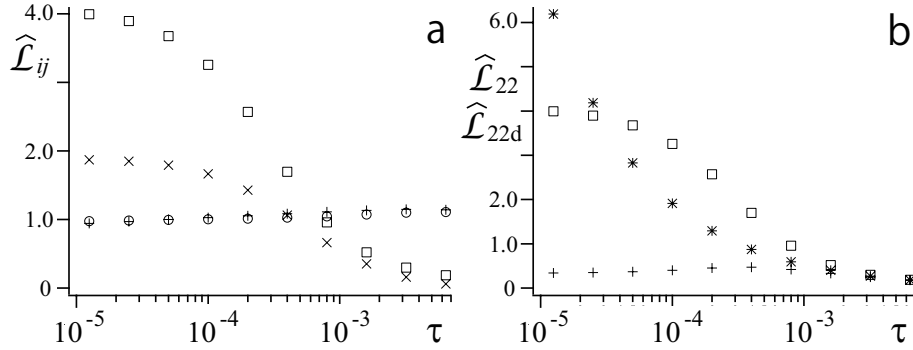


FIG. 3: Plots of the dimensionless Onsager coefficients against the reduced temperature τ for a mixture of LW. (a) The symbols \circ , \times , and \square represent $\hat{\mathcal{L}}_{11}$, $\hat{\mathcal{L}}_{12}$, and $\hat{\mathcal{L}}_{22}$, respectively, calculated by setting the surface field h equal to $0.1 \text{ cm}^3/\text{s}^2$. The symbol $+$, representing $\hat{\mathcal{L}}_{11}$ for $h = 0$, is obtained by replacing the dimensionless viscosity $\hat{\eta}(\hat{r})$ with its value at the critical composition irrespective of \hat{r} . (b) The symbol \square represents $\hat{\mathcal{L}}_{22}$, and is a replot of the same symbol in (a). The symbol $+$ represents $\hat{\mathcal{L}}_{22d}$, which is a part of $\hat{\mathcal{L}}_{22}$, for $h = 0.1 \text{ cm}^3/\text{s}^2$, whereas the symbol $*$ represents $\hat{\mathcal{L}}_{22d}$ for $h = 0$.

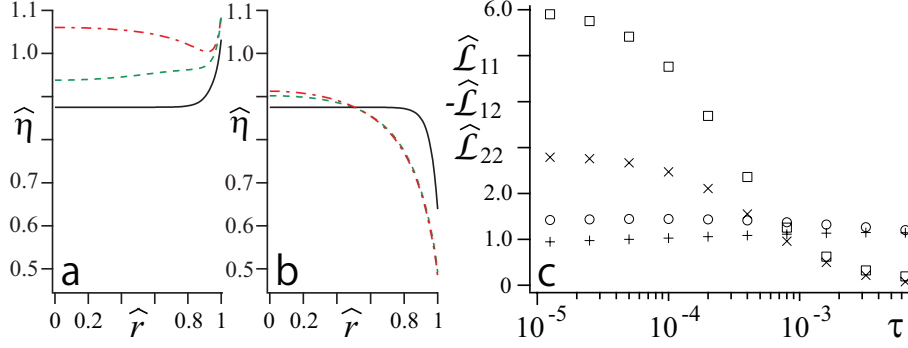


FIG. 4: We use $h = 0.1 \text{ cm}^3/\text{s}^2$ in (a) and $h = -0.1 \text{ cm}^3/\text{s}^2$ in (b) to plot the dimensionless viscosity $\hat{\eta}(\hat{r})$ for a mixture of LW against \hat{r} . The black solid, green dashed, red dash-dot curves represent the results for $\tau = 6.4 \times 10^{-3}$, 4.0×10^{-4} , and 1.25×10^{-5} , respectively. For these values of τ , $\hat{\eta}$ takes 0.875, 0.922 and 1.06 at the critical composition, respectively. We use $h = -0.1 \text{ cm}^3/\text{s}^2$ to plot $\hat{\mathcal{L}}_{11}$ (\circ), $-\hat{\mathcal{L}}_{12}$ (\times), and $\hat{\mathcal{L}}_{22}$ (\square) against τ in (c). For comparison, the same results as shown by the cross in Fig. 3(a) are here replotted with the same symbol.

way. For the two smallest values of τ , η_s changes less in Fig. 4(a) for $h > 0$ than in Fig. 4(b) for $h < 0$ because c_a in the tube is larger than c_{ac} for $h > 0$ and the red dash-dot curve has the nearly flat portion in Fig. 2(a). Thus, the results for $h > 0$ (\circ) and the ones for $h = 0$ ($+$) approximately agree in Fig. 3(a), and not in Fig. 4(c). In this figure, $\hat{\mathcal{L}}_{12}$ becomes negative because of $\hat{\psi}^{(0)} < 0$ in Eq. (48), whereas $\hat{\mathcal{L}}_{22}$ is positive because of Eqs. (42) and (47). In Figs. 3(a) and 4(c), $|\hat{\mathcal{L}}_{12}|$ and $\hat{\mathcal{L}}_{22}$ increases as τ decreases in the presence of PA, because $|\hat{\psi}^{(0)}(\mathbf{r})|$ in $\Omega_1[1]$ and $\Omega_1[\hat{\psi}^{(0)}]$ then increases (Fig. 10(a)). When the sign of $h(\neq 0)$ is changed at a value of τ , the value of $|\hat{\mathcal{L}}_{ij}|$ does not remain the same because of the asymmetry of the background part of η_s in Fig. 2(a). Then, $\hat{\mathcal{L}}_{22d}$ remains unchanged owing to Eqs. (42) and (47). When we set $\delta P = 0$ and $\delta c_a < 0$, which gives $(\delta\mu)_P = \delta\mu < 0$ owing to Eq. (7), the total mass flow enters into the right (left) reservoir through the tube with $h > 0$ ($h < 0$) because of Eq. (50) and $\hat{\mathcal{L}}_{12} > 0$ ($\hat{\mathcal{L}}_{12} < 0$). This flow direction is reasonable, considering that it would relax the mass-fraction difference between the reservoirs because the component a is concentrated in (depleted from) the tube with $h > 0$ ($h < 0$).

B. Onsager coefficients for a mixture of NEMP

We consider a mixture of NEMP near the upper critical consolute point ($T_c = 300$ K and $c_{ac} = 0.466$), taking nitroethane to be the component a. The ratio ρ_{bc}/ρ_{ac} is closer to unity than the ratio for a mixture of LW. We have $\xi_0 = 2.30 \times 10^{-1}$ nm [43] to obtain $\tau_* = 6.49 \times 10^{-5}$. The estimate of C_2 in Appendix C gives $\psi_* = 4.19 \times 10$ kg/m³, which leads to $\mu_* = 1.50 \times 10^{-2}$ m²/s². We use the experimental data of Refs. [43, 51] to obtain $\eta_* = 5.10 \times 10^{-4}$ Pa·s and dependence of η_s on τ and ψ in Appendix E. The dependence is shown in Fig. 5(a), where the range of values of η_s at a value of τ is narrower than the one at any value of τ in Fig. 2(a). The fitted curve in the former figure shifts upward as τ decreases, unlike the fitted curve in the latter figure, which shows data near the lower consolute point. The peak due to the singular part is clearer in the former figure. As in Fig. 2(b), we plot ρ against c_a in the inset of Fig. 5(a), where data from Ref. [52] and the fitted curve are shown. The curve-fit gives $\bar{v}_a^{(\text{ref})} = 9.60 \times 10^{-4}$ m³/kg and $\bar{v}_b^{(\text{ref})} = 1.53 \times 10^{-3}$ m³/kg, which yield $\rho_c = 7.92 \times 10^2$ kg/m³ and $\varphi_c = -5.46 \times 10$ kg/m³. In the following calculations, $|c_a - c_{ac}|$ in the tube at equilibrium is smaller than 0.17.

The components of $\hat{\mathcal{L}}$ are calculated using Eqs. (47) and (48). As τ decreases, $\hat{\mathcal{L}}_{12} = \hat{\mathcal{L}}_{21}$ becomes positively larger in Fig. 5(b) for $h > 0$ and negatively larger Fig. 5(c) for $h < 0$. Then, in either of the figures, $\hat{\mathcal{L}}_{22}$ more eminently increases, whereas $\hat{\mathcal{L}}_{11}$ and $\hat{\mathcal{L}}_{22d}$ exhibit much less distinct changes. At $\tau = 1.25 \times 10^{-5}$ for $h = 0$, $\hat{\mathcal{L}}_{22d}$ equals 7.08, which is much larger than the corresponding value for $|h| = 0.1$ cm³/s², shown by the cross on the extreme left in Fig. 5(b). Thus, the eminent increase of $\hat{\mathcal{L}}_{22}$ shown in each of Figs. 5(b) and (c) is not caused by the critical enhancement of Λ . These properties are qualitatively the same as shown in Figs. 3(a) and 4(c). The value shown by the circle on the extreme left in Fig. 5(b) changes to 0.935 when h vanishes. This change is larger in magnitude than the corresponding change in Fig. 3(a) for a mixture of LW, owing to the clear peak of η_s in Fig. 5(a).

C. Mass flow rates

We have $\psi_* \bar{v}_-^{(\text{ref})} = 6.00 \times 10^{-4}$ in a mixture of LW and -1.18×10^{-2} in a mixture of NEMP. In the presence of PA, $\left| \hat{\mathcal{L}}_{12} \right|$ is larger than approximately one thirds of $\hat{\mathcal{L}}_{22}$ in

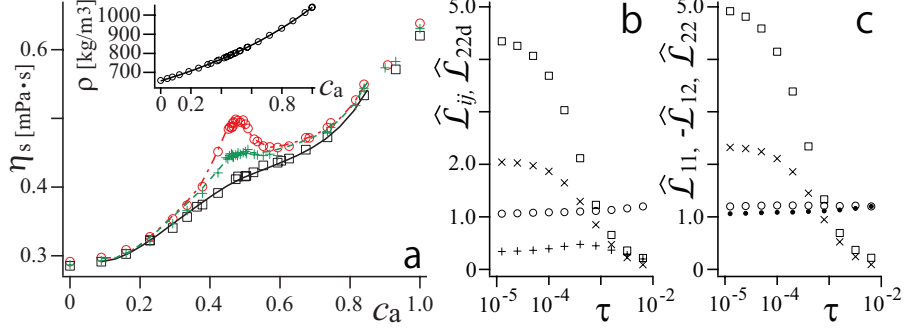


FIG. 5: (a) Experimental data for a mixture of NEMP; c_a denotes the mass fraction of nitroethane. We shift the data of viscosity at $\tau = 1.47 \times 10^{-4}$, 1.82×10^{-3} , and 1.19×10^{-2} of Ref. [51], as mentioned in Appendix E, to plot the results with red circles, green crosses, and black squares, respectively. Curve-fits for $0.08 < c_a < 0.85$ yield the red dash-dot, green dashed, and black solid curves for the respective values of τ . In the inset, the circle represents experimental data from Ref. [52] for the relationship between ρ and c_a at 300.153 K. The solid curve is obtained by curve fitting to the data for $0.3 < c_a < 0.6$, as in Fig. 2(b). (b, c) Calculation results of the components of $\hat{\mathcal{L}}$ are plotted against τ for a mixture of NEMP. The symbols \circ , \times , \square , and $+$ in (b) represent $\hat{\mathcal{L}}_{11}$, $\hat{\mathcal{L}}_{12}$, $\hat{\mathcal{L}}_{22}$, and $\hat{\mathcal{L}}_{22d}$, respectively, for $h = 0.1 \text{ cm}^3/\text{s}^2$. The symbols \circ , \times , and \square in (c) represent $\hat{\mathcal{L}}_{11}$, $-\hat{\mathcal{L}}_{12}$, and $\hat{\mathcal{L}}_{22}$, respectively, for $h = -0.1 \text{ cm}^3/\text{s}^2$. For comparison, the same results as shown by the circle in (b) are replotted with the solid circle in (c).

Figs. 3(a), 4(c), 5(b), and 5(c). Thus, for these results under $h \neq 0$, the second terms in the two pairs of parentheses in Eq. (49) are negligible and Eq. (49) can be approximated to be

$$-\frac{\mathcal{I}_* \rho_n^{(\text{ref})}}{\mu_* \psi_*} \hat{\mathcal{L}}_{11} \mp \frac{\mathcal{I}_*}{2\mu_*} \hat{\mathcal{L}}_{21}. \quad (51)$$

Here, owing to $\psi_* \ll \rho_n^{(\text{ref})} = \rho_{nc}$, the first term is predominant for the values of $\hat{\mathcal{L}}_{11}$ and $\hat{\mathcal{L}}_{12}$ in the figures mentioned above. For these values, the first term is predominant in Eq. (50) unless h vanishes, although $\hat{\mathcal{L}}_{22}$ is larger than $|\hat{\mathcal{L}}_{12}|$ as far as examined. We define a dimensionless mass flow rate of the component n as

$$\frac{d\hat{\mathcal{M}}_{nR}}{d\hat{t}} \equiv \frac{1}{\rho_c \mathcal{I}_*} \frac{d\mathcal{M}_{nR}}{dt}. \quad (52)$$

A dimensionless total mass flow rate, denoted by $d\hat{\mathcal{M}}_R/(d\hat{t})$, is defined as the sum of Eq. (52) over $n = a$ and b , and is equal to $\hat{\mathcal{I}}$. Below, in flow driven by the pressure difference,

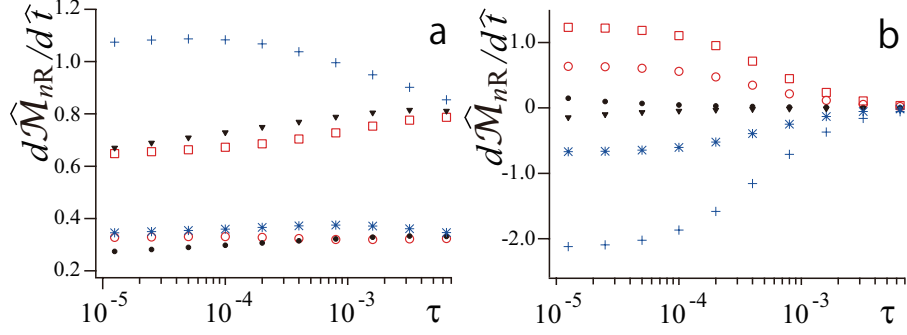


FIG. 6: Plots of the dimensionless mass flow rates against τ for a mixture of LW; $d\hat{\mathcal{M}}_{\text{aR}}/(dt)$ is plotted with red open circles, solid circles, and blue asterisks, whereas $d\hat{\mathcal{M}}_{\text{bR}}/(dt)$ with red squares, solid triangles, and blue crosses. The values of open circles and squares are obtained for $h = 0.1 \text{ cm}^3/\text{s}^2$, those of solid circles and triangles for $h = 0$, and those of asterisks and crosses for $h = -0.1 \text{ cm}^3/\text{s}^2$. We set $(\delta P, (\delta\mu)_P)$ to be $(-\mu_*\psi_*, 0)$ in (a), and $(0, -\mu_*)$ in (b).

we calculate $c_{\text{aR}}^{(\text{flux})}$, which is defined as the ratio of Eq. (52) with $n = \text{a}$ to $d\hat{\mathcal{M}}_{\text{R}}/(dt)$. This ratio can be interpreted as the mass fraction of the component a in a mixture flowing into the right reservoir per unit time when the mass flow rates of the components share the same sign, becoming equal to c_{ac} when the second term of Eq. (49) vanishes.

For a mixture of LW, the dimensionless mass flow rates under $(\delta P, (\delta\mu)_P) = (-\mu_*\psi_*, 0)$ are calculated by using Eq. (49) and plotted in Fig. 6(a). For $h > 0$, the mass flow rate of the component a is less dependent on τ than that of b, as shown by open circles and squares. This is consistent with Fig. 4(a), where the curves of $\hat{\eta}$ are close to each other in the neighborhood of the tube wall attracting the component a. For these mass flow rates, $c_{\text{aR}}^{(\text{flux})}$ increases from 0.291 to 0.336 as τ decreases from 6.4×10^{-3} to 1.25×10^{-5} . The deviation from c_{ac} is mainly caused by the second term in Eq. (51), and $c_{\text{aR}}^{(\text{flux})} > c_{\text{ac}}$ can be realized intuitively because $h > 0$ means the absorption of the component a in the tube. For $h = 0$, noting $\hat{\mathcal{L}}_{12} = \hat{\mathcal{L}}_{21} = \hat{\mathcal{L}}_{22\text{v}} = 0$, we substitute the values of the crosses in Fig. 3(a) and those of the asterisks in Fig. 3(b) into $\hat{\mathcal{L}}_{11}$ and $\hat{\mathcal{L}}_{22}$ of Eq. (49), respectively, to obtain the results shown by the solid circle and triangle in Fig. 6(a). They decrease as τ decreases, in particular for small τ , which is attributed to the change of the first term of Eq. (51) due to the weak critical enhancement of η_{s} . For them, because the second term of Eq. (51) vanishes, $c_{\text{aR}}^{(\text{flux})}$ remains close to c_{ac} , ranging from $c_{\text{ac}} = 0.2900$ to 0.2901. For

$h < 0$, the results are shown by the asterisk and cross in Fig. 6(a), and $c_{\text{aR}}^{(\text{flux})}$ decreases from 0.289 to 0.243 as τ decreases from 6.4×10^{-3} to 1.25×10^{-5} . They show $c_{\text{aR}}^{(\text{flux})} < c_{\text{ac}}$ because $h < 0$ means the depletion of the component a from the tube. The value shown by the cross noticeably increases as τ decreases from $\tau = 6.4 \times 10^{-3}$ to $\tau = 4.0 \times 10^{-4}$ in Fig. 6(a), which is consistent with the results of $\hat{\eta}$ in Fig. 4(b). In this figure, the dashed and dash-dot curves are distinctly below the solid curve in the neighborhood of the tube wall attracting the component b.

For a mixture of LW, the dimensionless mass flow rates under $(\delta P, (\delta\mu)_P) = (0, -\mu_*)$ are calculated by using Eq. (50) and plotted in Fig. 6(b). The results for $h > 0$, shown by the open circle and square, increase distinctly as τ decreases. At $\tau = 1.25 \times 10^{-5}$, the ratio of the first term of Eq. (50) to its total is 0.851 for the component a and the ratio for b is 1.07. These values are rather close to unity, indicating that the first term is dominant. In the absence of PA, we have $\hat{\mathcal{L}}_{12} = \hat{\mathcal{L}}_{22v} = 0$, and the total mass flow rate vanishes. This can be read from the results shown by the solid circle and triangle in Fig. 6(b). They increase in magnitude as τ decreases, which represents the critical enhancement of Λ . The results for $h < 0$, shown by the asterisk and cross, become negatively larger as τ decreases in Fig. 6(b). At $\tau = 1.25 \times 10^{-5}$, the ratio of the first term of Eq. (50) to its total is 1.21 for the component a and the ratio for b is 0.937. These values indicate the predominance of the first term. Thus, the total mass flow rate is positively (negatively) larger for $h > 0$ ($h < 0$) as τ decreases, which is expected from the change of $\hat{\mathcal{L}}_{12}$ in Fig. 3(a) (Fig. 4(c)) and implies that diffusioosmosis is caused by the PA.

Qualitatively, the dimensionless mass flow rates for a mixture of NEMP share many properties with those for a mixture of LW. For that mixture, the dimensionless mass flow rates under $(\delta P, (\delta\mu)_P) = (-\mu_*\psi_*, 0)$ and $(\delta P, (\delta\mu)_P) = (0, -\mu_*)$ are plotted in Figs. 7(a) and (b), respectively. In the former, for the results shown by the open circle and square ($h > 0$), $c_{\text{aR}}^{(\text{flux})}$ increases from 0.467 to 0.516 as τ decreases from 6.4×10^{-3} to 1.25×10^{-5} . The results for $h = 0$, shown by the solid circle and triangle in Fig. 7(a), decrease as τ decreases. For these values, $c_{\text{aR}}^{(\text{flux})}$ remains close to c_{ac} , ranging from 0.463 to $c_{\text{ac}} = 0.466$. For $h < 0$, the results are shown by the asterisk and cross in Fig. 7(a), and $c_{\text{aR}}^{(\text{flux})}$ decreases from 0.463 to 0.414 as τ decreases from 6.4×10^{-3} to 1.25×10^{-5} . In Fig. 7(b), the results for $h > 0$,

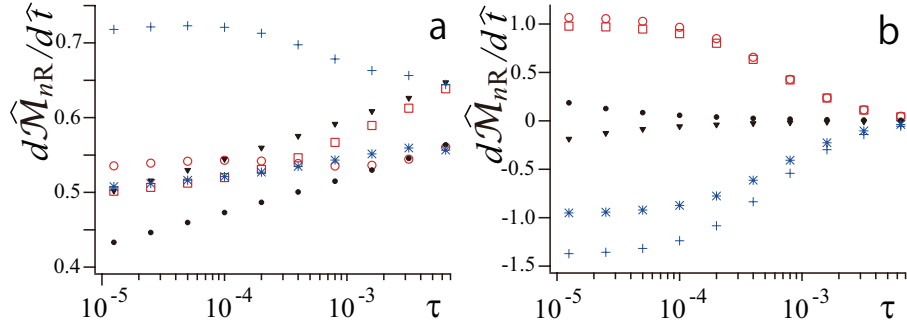


FIG. 7: Plots of $d\hat{\mathcal{M}}_{nR}/(d\hat{t})$ against τ for a mixture of NEMP, corresponding with Fig. 6. The symbols in (a) and (b) have the same meanings as the ones in (a) and (b) in Fig. 6, respectively.

shown by the open circle and square, increase eminently as τ decreases. At $\tau = 1.25 \times 10^{-5}$, the ratio of the first term of Eq. (50) to its total is 0.893 for the component a and the ratio for b is 1.12. The magnitudes of the results for $h = 0$, shown by the solid circle and triangle in Fig. 7(b), increase as τ decreases, and the total mass flow rate vanishes. The results for $h < 0$, shown by the asterisk and cross in Fig. 7(b), become negatively larger as τ decreases. The ratio of the first term of Eq. (50) to its total is 1.14 for the component a and the ratio for b is 0.906. The magnitude of the total mass rate increases with decreasing τ for $h \neq 0$, which implies that diffusioosmosis is caused by the PA.

D. Diffusioosmosis

The first two terms on the RHS of Eq. (17) can be rewritten as $-\nabla(p + \varphi_c \mu) - \psi \nabla \mu$ with the aid of Eq. (31). The sum $p + \varphi_c \mu$ represents a scalar pressure, which keeps the incompressibility at the order of ε . In the presence of PA, the term $-\psi \nabla \mu$ becomes nonzero to cause diffusioosmosis when a gradient of μ is imposed. Being significant under the mass-fraction difference, this mechanism also works under the pressure difference to yield a slight contribution, as shown by the second term in the first parenthesis of Eq. (49). In the linear regime considered in the present study, we define G so that

$$\frac{1}{\rho_c} \frac{d\mathcal{M}_R}{dt} = -G \frac{\delta c_a}{c_{ac} L_{\text{tube}}} \quad (53)$$

holds. Here, the LHS equals the flow rate \mathcal{I} caused by the mass-fraction difference δc_a , with δP setting equal to zero, whereas the fraction on the RHS is the composition gradient normalized by c_{ac} . Thus, G represents the conductance in diffusioosmosis and equals

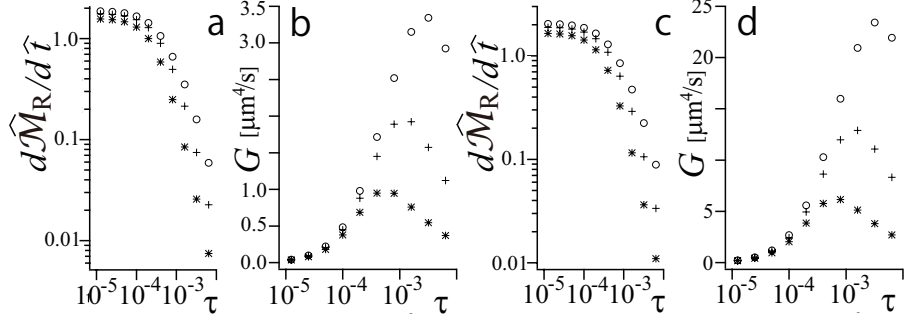


FIG. 8: We plot the dimensionless total mass flow rate $d\hat{\mathcal{M}}_R/d\hat{t}$ for $(\delta P, (\delta\mu)_P) = (0, -\mu_*)$ in (a) and the conductance G in (b) against τ for a mixture of LW. Those for a mixture of NEMP are plotted in (c) and (d), respectively. Circles, crosses, and asterisks represent the results obtained by setting the surface field h equal to 0.1, 0.032, and 0.01 cm^3/s^2 , respectively. The result at a value of τ for $h = 0.1 \text{ cm}^3/\text{s}^2$ in (a) is the sum of the results shown by the open circle and square at the value of τ in Fig. 6(b). The same relationship holds between the results in (c) and Fig. 7(b).

the product of Eq. (34) and $\mathcal{I}_* c_{ac} L_{\text{tube}} \hat{L}_{12} / \mu_*$, where \hat{L}_{12} equals $d\hat{\mathcal{M}}_R/(d\hat{t}) \equiv \hat{\mathcal{I}}$ under $(\delta P, (\delta\mu)_P) = (0, -\mu_*)$. The signs of G and h are the same because of the discussion on Figs. 6(b) and 7(b). As shown in Fig. 8(a) for a mixture of LW and Fig. 8(c) for a mixture of NEMP, the dimensionless total mass flow rate for $h > 0$ increases as τ decreases, and appears to reach a plateau for small τ . The increase is due to that of the adsorption layer's thickness, which is caused by that of the osmotic susceptibility. The plateau would come from the finite size of the tube's cross section. The increase of the susceptibility also reduces $|(\delta\mu)_P|$ under a given value of δc_a , and hence G decreases for small τ in Figs. 8(b) and (d) for $h > 0$. Owing to the plateau mentioned above, Eq. (34), and Eq. (40), G is approximately proportional to τ^γ for small τ . For each value of h , G has a peak in these figures. The value of τ at the peak decreases as h decreases, because then occurrence of the plateau is limited to smaller values of τ in Figs. 8(a) and (c). For a value of h , the maximum of G in the latter figure are larger than the one in the former because η_s takes smaller values in a mixture of NEMP than in a mixture of LW.

Suppose that $L_{\text{tube}} = 10 \text{ }\mu\text{m}$ and $\delta c_a = -c_{ac}/10$. If we adopt $G = 3 \text{ }\mu\text{m}^4/\text{s}$ from Fig. 8(b), Eq. (53) becomes equal to $0.03 \text{ }\mu\text{m}^3/\text{s}$. Because of $r_{\text{tube}} = 0.1 \text{ }\mu\text{m}$, the average of v_z across the tube's cross-section is approximately $1 \text{ }\mu\text{m}/\text{s}$, which could be detected experimentally.

It is shown at the end of Appendix D that the average for large τ and small $|h|$ can be approximately calculated using the Gaussian model. As τ increases well beyond the range of Fig. 8, ξ near the tube wall approaches a molecular size and the RHS of Eq. (34) should stop increasing in proportion to τ^γ because of the background contribution to the osmotic susceptibility [46, 53]. Then, our coarse-grained description would fail and diffusioosmosis should be explained in terms of the conventional mechanism rather than the PA [33, 34, 54].

VI. SUMMARY AND FURTHER DISCUSSION

Assuming that the free-energy functional is given by Eq. (8), that the tube is not necessarily cylindrical but has the same cross section anywhere, and that the mixture at equilibrium has either critical or near-critical composition in the central region of the reservoir, we derive some properties on the Onsager coefficients, appearing in Eq. (3), in Section III. As is well expected, the pressure difference δP causes the total mass flow rate with a mixture flowing out of the tube being rich in the adsorbed component. The mass-fraction difference δc_a can cause the total mass flow, *i.e.*, diffusioosmosis emerges, only in the presence of PA. The Onsager coefficients \mathcal{L}_{21} and \mathcal{L}_{12} , which are equal to each other owing to the reciprocal relation, are involved with these effects of PA, respectively. The coefficient \mathcal{L}_{22} is separated into two parts; \mathcal{L}_{22v} involves the convection and \mathcal{L}_{22d} involves the interdiffusion. The former becomes nonzero only in the presence of PA.

In the presence of PA, the homogeneity at equilibrium is broken, and the first two terms on the RHS of Eq. (17) cannot be unified into a gradient of some scalar pressure. This makes $\mathcal{L}_{12} = \mathcal{L}_{21}$ and \mathcal{L}_{22v} nonzero. Thus, these effects of PA comes from the reversible part of the pressure tensor, Π_{rev} . The transport coefficients are introduced in relating irreversible fluxes linearly with thermodynamic forces defined in the bulk of a fluid; η_s relates the viscous stress with the rate-of-strain tensor and Λ relates the difference between the diffusion fluxes of the components with the difference between the chemical potentials [16, 55]. Whether the PA is present or not, Curie's principle prohibits the viscous stress and the diffusive flux from being linearly related with the gradient of chemical potential and with the velocity gradient, respectively [16]. The prohibition can be also explained by the difference in the parity concerning the time-reversal symmetry between \mathbf{v} and φ [56].

To evaluate the effects of PA quantitatively, we use the free-energy functional coarse-grained in the renormalized local functional theory [12]. We calculate the Onsager coefficients by assuming the tube to be cylindrical and assuming the mixture at equilibrium to have the critical composition in the central region of the reservoir; their expressions are shown in Section IV C. In this model, δP is not always equal to δp , as mentioned at Eq. (32). In the absence of PA, the Hagen-Poiseuille flow is generated under the pressure difference ($\delta P \neq 0$ and $\delta c_a = 0$), with the interdiffusion being usually accompanied, whereas the interdiffusion without the total mass flow is generated by the mass-fraction difference ($\delta P = 0$ and $\delta c_a \neq 0$). The effects of PA mentioned in the first paragraph of this section are numerically confirmed; the dimensionless Onsager coefficients, introduced at Eq. (45), are plotted in Figs. 3(a), 4(c), 5(b), and 5(c), whereas the dimensionless mass flow rates, introduced at Eq. (52), are plotted in Figs. 6 and 7. In the diffusioosmosis due to PA, the total mass of a mixture flows into the reservoir with a smaller composition of the preferred component, as in the conventional diffusioosmosis [21, 33]. However, their mechanisms are different, as mentioned in the fourth paragraph of Section I and at the beginning of Section V D. The conductance in diffusioosmosis due to PA, introduced at Eq. (53), exhibits a non-monotonic change with a peak as plotted against τ (Figs. 8(b) and (d)), owing to the opposing effects of the osmotic susceptibility on the conductance mentioned below Eq. (53). The critical enhancement of the transport coefficients is evaded by the PA.

In the calculation above, the difference in the parentheses of Eq. (28) equals $\psi^{(0)}$. For our results of the Onsager coefficients to be meaningful for $h \neq 0$, $\psi^{(0)}$ is required to be much larger than $\varepsilon\psi^{(1)}$ somewhere in the tube. Considering that ψ is changed from $\psi^{(0)}$ by the velocity field, this requirement can be simplified in terms of a typical energy per unit area as $\eta_s U \ll |h\psi^{(0)}(r_{\text{tube}})|$, where U is a typical speed of the velocity field and can be taken as the average of v_z across the tube's cross-section. The RHS of this inequality is larger than approximately 10^{-6} kg/s² in Fig. 10(a), where $\hat{\psi}^{(0)}$ is calculated with some sets of values of τ and h for a mixture of LW; this value of the lower bound is obtained from the value of $\hat{\psi}^{(0)}(1)$ for $\tau = 4.0 \times 10^{-4}$ and $h = 0.01$ cm³/s². Thus, for the sets of values, the requirement is met when the average of v_z is much smaller than approximately 400 $\mu\text{m/s}$. This value is approximately the same for a mixture of NEMP under the same sets of values of τ and

h although data not shown. Then, the Reynolds number, with $r_{\text{tube}} = 10^{-1} \mu\text{m}$ taken as a typical length, is much smaller than unity, which is also required in the linear regime. Considering $\hat{\psi}^{(0)}(1)$ can be roughly approximated to be unity in Fig. 10(a) we can nondimensionalize the typical speed by dividing it by $h\psi_*/\eta_*$ to use the quotient as the smallness parameter. Judging from the velocity profile shown in Fig. 10(b), an estimate of U in flow driven by the pressure difference is given by the average of v_z in the Hagen-Poiseuille flow. An estimate of U in flow driven by the mass-fraction difference is given by Eq. (D3) when the approximation $\omega \approx \tau$ is valid and ξ at the critical composition is much smaller than r_{tube} .

Changes of the Onsager coefficients are continuous with respect to τ in our numerical results. When the mass fraction of the component disfavored by the tube wall is larger than its critical value at the central region of the reservoir in the reference state, the capillary condensation transition can occur in the tube at a value of τ [12, 57]. If this transition occurs as a first-order transition, the change in the Onsager coefficients should be discontinuous with respect to τ and exhibit hysteresis. Similar transitions have been reported for ion-containing mixtures [58–62]. It remains to be studied how the transport properties of a mixture in a tube change when it undergoes this kind of transition. The mass flow rates caused by the temperature difference between the reservoirs are also of interest. The renormalized local functional theory should be extended for this study so that it can describe the equilibrium density of a mixture’s entropy.

VII. CONCLUSIONS

In the isothermal transport of a mixture through a tube with the PA, the convective flow rich in the preferred component caused by the pressure difference is related via cross-effect Onsager coefficients with the total mass flow caused by the mass-fraction difference. The resulting diffusioosmosis has a mechanism involving the near-criticality, like diffusiophoresis in a near-critical mixture discussed recently by one of the present authors [34]. According to our numerical results, the critical enhancement of the transport coefficients is evaded by the PA, the conductance in diffusioosmosis changes non-monotonically with respect to the temperature, and the change is large enough to be detected experimentally.

Acknowledgments

The authors thank Prof. P. G. Wolynes for informing them of Ref. [18]. YF appreciates stimulating discussion with T. Iyori. S. Y. was supported by JSPS KAKENHI Grant-in-Aid for Young Scientists (B) (15K17737 and 18K13516).

Appendix A: Non-dissipative part of the stress tensor

As in conventional thermodynamics, we can derive the reversible part of the pressure tensor by considering the change of F due to an infinitesimal quasistatic deformation of a mixture [6, 8]. In this non-dissipative deformation, the chemical potentials μ_a and μ_b can be inhomogeneous, like an inhomogeneous magnetic field in a magnetic system. This means that each locus in a mixture has each particle bath. Here, unlike in the text, V_{tot} is the deformable region occupied by the mixture, t is not the time but a parameter of deformation, \mathbf{v} is the displacement of fluid particle per unit t , and \mathbf{j}_n represents the flux to the particle bath. The last implies that $\mathbf{j}_a + \mathbf{j}_b$ does not always vanish. Consider a small region, V_t , co-moving with the deformation. This region is assumed to have the smallest volume that allows us to define μ_n and Π_{rev} . They can be regarded as homogeneous over V_t . Below, the repeated indices are summed up. The local equilibrium in the bulk gives

$$\frac{d}{dt} \int_{V_t} d\mathbf{r} f_{\text{bulk}} = \mu_n \frac{d}{dt} \int_{V_t} d\mathbf{r} \rho_n(\mathbf{r}, t) - \Pi_{\text{rev}} : \int_{\partial V_t} dA \mathbf{n}_{\partial V_t} \mathbf{v}, \quad (\text{A1})$$

where the symbol $:$ represents the double dot product. Equation (A1) yields

$$\frac{Df_{\text{bulk}}}{Dt} + f_{\text{bulk}} \nabla \cdot \mathbf{v} = -\mu_n \nabla \cdot \mathbf{j}_n - \Pi_{\text{rev}} : (\nabla \mathbf{v}) \quad (\text{A2})$$

with the aid of Eq. (14). Here, D/Dt represents the Lagrangian “time-derivative”. Because V_{tot} also co-moves with the deformation, we have

$$\frac{dF}{dt} = - \int_{V_{\text{tot}}} d\mathbf{r} [\mu_n \nabla \cdot \mathbf{j}_n + \Pi_{\text{rev}} : (\nabla \mathbf{v})], \quad (\text{A3})$$

apart from a surface term, which involves f_{surf} . Here, μ_n and Π_{rev} can depend on \mathbf{r} .

We below outline how Eqs. (9) and (11) are derived from Eq. (8). The Lagrangian “time-derivative” of f_{bulk} is found to be the sum of

$$\frac{\partial f_{\text{bulk}}}{\partial \rho} \frac{D\rho}{Dt} + \frac{\partial f_{\text{bulk}}}{\partial (\nabla \rho)} \cdot \nabla \left(\frac{D\rho}{Dt} \right) - \frac{\partial f_{\text{bulk}}}{\partial (\nabla \rho)} \cdot (\nabla \mathbf{v}) \cdot (\nabla \rho) \quad (\text{A4})$$

and the above with ρ replaced by φ . Substituting this result into the LHS of Eq. (A2), and integrating the result over V_{tot} , we can transform the contribution from the bulk to $dF/(dt)$ into the form of the RHS of Eq. (A3) with μ_n and Π_{rev} given by Eqs. (9) and (11), except for a new surface term, which is generated by the application of the divergence theorem.

Below, $\nabla_{\parallel} \cdot \mathbf{v}_{\parallel}$ indicates the divergence defined on ∂V_{tot} and H_m denotes the mean curvature of ∂V_{tot} . The latter is defined so that it is positive when the center of curvature lies on the side directed by $\mathbf{n}_{\partial V_{\text{tot}}}$. The surface term unwritten in Eq. (A3) is combined with the new surface term. The combination gives the sum of

$$\int_{\partial V_{\text{tot}}} dA \frac{D\rho}{Dt} \left(\frac{\partial f_{\text{bulk}}}{\partial (\nabla\rho)} \cdot \mathbf{n}_{\partial V_{\text{tot}}} + \frac{\partial f_{\text{surf}}}{\partial \rho} \right), \quad (\text{A5})$$

the above with ρ replaced by φ , and

$$\int_{\partial V_{\text{tot}}} dA f_{\text{surf}} (\nabla_{\parallel} \cdot \mathbf{v}_{\parallel} - 2H_m \mathbf{v} \cdot \mathbf{n}_{\partial V_{\text{tot}}}) . \quad (\text{A6})$$

We can use Eq. (14) to rewrite the Lagrangian “time-derivatives” of the mass densities in terms of \mathbf{j}_n . This flux should not exist at ∂V_{tot} , where the particle bath does not exist. This means that the coefficients of the “time-derivatives” should vanish there, which leads to Eq. (19). Thus, this equation holds even in the dynamics [63]. Hence, the surface term unwritten on the RHS of Eq. (A3) is reduced to Eq. (A6), which means that $-f_{\text{surf}}$ works as a two-dimensional pressure in ∂V_{tot} . The force density $2f_{\text{surf}}H_m\mathbf{n}_{\partial V_{\text{tot}}}$ yields the Laplace pressure, as discussed in Appendix A of Ref. [64].

The reversible parts of the hydrodynamic equations contain nonlinear terms, as shown in Eqs. (11) and (16). The sum of the first two terms on the RHS of Eq. (17) equals the sum of $-\rho_n \nabla \mu_n$ over $n = \text{a}$ and b . Each term is linked with the first term on the RHS of Eq. (14) via the reciprocal relation after the hydrodynamic equations are linearized, as shown in Ref. [55]. This is expected to underlie the cross effects mentioned in Section III.

Appendix B: Reciprocal relation

We consider two sets of flow fields, each being driven by the thermodynamic forces $(-\delta P_k/T, -\delta \mu_k/T)$, with k being i or ii. The resultant thermodynamic fluxes and fields in the tube are also indicated by the subscript k . Different ways of applying the divergence

theorem to the volume integral of $\eta_0 E_i^{(1)} : E_{ii}^{(1)}$ over the tube interior, denoted by V_{tube} , yield

$$\int_{V_{\text{tube}}} d\mathbf{r} \mathbf{v}_{ii}^{(1)} \cdot \left[\nabla \cdot \left(\eta_0 E_i^{(1)} \right) \right] = \int_{V_{\text{tube}}} d\mathbf{r} \mathbf{v}_i^{(1)} \cdot \left[\nabla \cdot \left(\eta_0 E_{ii}^{(1)} \right) \right] , \quad (\text{B1})$$

where we note that the no-slip boundary condition is imposed at the tube wall, that $\nabla \cdot \mathbf{v}_k^{(1)}$ vanishes in a stationary laminar flow in the tube, and that effects of the tube edges are assumed to be negligible. Substituting Eq. (17) into Eq. (B1), we use Eq. (27) to find that

$$\frac{\delta P_i - \varphi_c \delta \mu_i}{\rho^{(\text{ref})} L_{\text{tube}}} \int_{S_{\text{tube}}} dA \rho^{(0)} v_{iiz}^{(1)} + \frac{\delta \mu_i}{L_{\text{tube}}} \int_{S_{\text{tube}}} dA \varphi^{(0)} v_{iiz}^{(1)} \quad (\text{B2})$$

equals the above equation with the subscripts i and ii exchanged. Putting $\delta \mu_i$ and δP_{ii} equal to zero, we have $\mathcal{L}_{ii} \delta P_i = \mathcal{J}_i \delta \mu_{ii}$ because j_{iz} vanishes. Thus, $\mathcal{L}_{12} = \mathcal{L}_{21}$ is derived. This derivation remains valid even when $\rho^{(0)}$ is inhomogeneous, unlike that of Ref. [19].

Appendix C: Renormalized local functional theory

The composition profile in a mixture has the probability density in equilibrium fluctuations. The effective Hamiltonian is defined in such a way that the exponential of its negative is proportional to the probability density functional. As a bare model for the bulk of a mixture, we can assume the effective Hamiltonian of the Ginzburg-Landau-Wilson type, or the ψ^4 model, for the order-parameter. Near the critical point, the bare model gives nearly the same probabilities, close to the maximum probability, to many composition profiles, which differ from each other only by details with length scales smaller than the local correlation length, and hence remarkable composition fluctuations arise over these scales. Changing the way of counting profiles to neglect fine differences between profiles, we can unify many profiles into much fewer profiles. That is, coarse-graining ψ up to the local correlation length enables us to regard the average profile as maximizing the resultant probability density functional, which is called renormalized local functional [12]. The ψ -dependent part of the coarse-grained effective Hamiltonian for the bulk of a mixture with $\mu = 0$ is given by the volume integral of the sum of

$$\frac{1}{2} C_1 \xi_0^{-2} \omega^{\gamma-1} \tau \psi^2 + \frac{1}{12} C_1 C_2 \xi_0^{-2} \omega^{\gamma-2\beta} \psi^4 , \quad (\text{C1})$$

and $C_1 \omega^{-\nu} |\nabla \psi|^2 / 2$ over V_{tot} . Here, C_1 is a positive nonuniversal constant and C_2 is given by $C_2 = 3u^* C_1 \xi_0$. The quantity ω , defined by Eq. (35), satisfies a self-consistent condition,

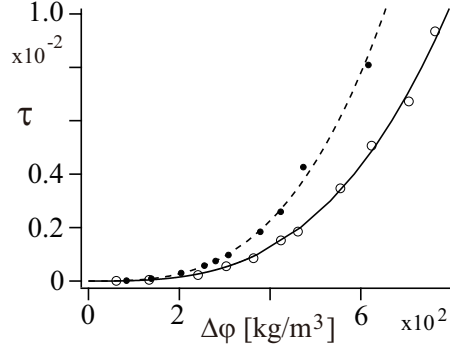


FIG. 9: Relationship between τ and the difference in φ between coexistence phases, denoted by $\Delta\varphi$, in a mixture. The open and solid circles are replots of data in Ref. [66] for a mixture of LW and data in Ref. [67] for a mixture of NEMP, respectively. The solid and dashed curves are obtained by the curve-fits of twice the value of Eq. (3.3) of Ref. [12] to these sets of data, respectively.

$\omega = \tau + C_2\omega^{1-2\beta}\psi^2$, because the mean-field approximation is valid after coarse-graining up to ξ . The logarithm of the probability density is proportional to Eq. (18) divided by $-k_B T$. Thus, we can identify $f_-(\psi) - (\mu_-)_c\varphi$ with the product of $k_B T$ and Eq. (C1), and identify $M_-(\psi)$ with $k_B T C_1 \omega^{-\eta\nu}$.

Estimates of C_2 are obtained as follows. The linear relationship between the refractive index and the volume fraction in a mixture of LW are shown in Fig. 2 of Ref. [66]. Using the three values of the circles in this figure and the index of the pure water, 1.330, we obtain the fitted line with the slope of 1.77×10^{-1} . Reference [66] also shows the refractive indices of the coexistent two phases above the lower consolute temperature. Converting the difference between the indices into the one in φ with the aid of the values of $\bar{v}_h^{(\text{ref})}$ mentioned in the text, we plot the relationship between the latter difference ($\Delta\varphi$) and τ in Fig. 9. The coexistence curve for $\mu = 0$ is given by Eqs. (3.3) and (3.23) of Ref. [12], and the data are approximately regarded as obtained for $\mu = 0$. The curve-fit to the data yields $C_2 = 7.14 \times 10^{-7} \text{ m}^6/\text{kg}^2$ for a mixture of LW. For a mixture of NEMP, we obtain the relationship between $\Delta\varphi$ and τ from data (Run A) of Ref. [67] and find $C_2 = 1.05 \times 10^{-6} \text{ m}^6/\text{kg}^2$ (Fig. 9).

Appendix D: Composition profiles and flow profiles

Applying the procedure mentioned in the last paragraph of Section II B, we find that $\hat{\psi}^{(0)}(\hat{r})$ is the solution of the differential equation for $\hat{\psi}(\hat{r})$,

$$0 = \hat{f}'(\hat{\psi}) - \frac{1}{2} \frac{d\hat{\omega}^{-\eta\nu}}{d\hat{\psi}} \left(\partial_{\hat{r}} \hat{\psi} \right)^2 - \hat{\omega}^{-\eta\nu} \left(\partial_{\hat{r}}^2 + \frac{1}{\hat{r}} \partial_{\hat{r}} \right) \hat{\psi} \quad \text{for } \hat{r} < 1, \quad (\text{D1})$$

where $\hat{\omega}$ is regarded as a function of $\hat{\psi}$ via Eq. (39), together with the boundary condition, $\partial_{\hat{r}} \hat{\psi} = \hat{h} \hat{\omega}^{\eta\nu}$ at $\hat{r} = 1$, with \hat{h} being defined as $hT^*/(T\mu_*r_{\text{tube}})$. These equations indicate that the sign of $\hat{\psi}^{(0)}$ is changed by changing that of h . We use these equations and Eq. (43) to obtain Fig. 10 for a mixture of LW. Because $h > 0$ is assumed, $\hat{\psi}^{(0)}$ is positive and increases toward the wall in Fig. 10(a). As τ decreases for $h = 0.1 \text{ cm}^3/\text{s}^2$, $\hat{\psi}^{(0)}$ increases throughout the tube, which can be interpreted as thickening of the adsorption layer. Using $\hat{\psi}^{(0)}(\hat{r})$ for $\hat{\psi}$ in Eq. (39), we calculate $\hat{\xi}$, defined as ξ/r_{tube} , with the aid of Eq. (35). Its smallest value in the inset of Fig. 10(a) gives $\xi = 3 \text{ nm}$, which is sufficiently large as compared with a molecular size. This is required in our coarse-grained description.

By setting $(\delta\hat{P}, \delta\hat{\mu}) = (-\varepsilon, 0)$ for a mixture of LW, we calculate $v_z^{(1)}$ and plot the results in Fig. 10(b), where $\hat{v}_z^{(1)}$ is a dimensionless quantity defined as $v_z^{(1)}$ divided by $8\mathcal{L}_*/(\pi r_{\text{tube}}^2) = 2.64 \text{ } \mu\text{m/s}$. The quantity decreases with τ , which is consistent with the increase of η_s in Fig. 4(a). Owing to the slight change of η_s , the quantity does not so much deviate from the black dotted curve, which is obtained by setting $\hat{\eta}$ to unity and represents the Hagen-Poiseuille flow, $\hat{v}_z^{(1)} = (1 - \hat{r}^2)/4$. Setting $\delta\hat{P}$ as above and $\delta\hat{\mu}$ equal to not zero but $-\hat{\mathcal{L}}_{11}\delta\hat{P}/\hat{\mathcal{L}}_{12} = \varepsilon\hat{\mathcal{L}}_{11}/\hat{\mathcal{L}}_{12}$ to make $\hat{\mathcal{I}}$ vanish at $\tau = 1.25 \times 10^{-5}$, we calculate $\hat{v}_z^{(1)}$ and plot the result with the red thicker dash-dot-dot curve in Fig. 10(b). It is positive near the tube center, and negative in an outer region, where the effect of $\delta\hat{\mu}$ exceeds that of $\delta\hat{P}$. This kind of bidirectional flow is also pointed out in Ref. [17]. In Fig. 10(c), $\hat{v}_z^{(1)}$ for $(\delta\hat{P}, \delta\hat{\mu}) = (0, -\varepsilon)$ increases as the adsorption is stronger. At the largest value of τ , the cylindrical shape of the tube has little effect on the convection, and $\hat{v}_z^{(1)}$ appears to change only near the tube wall, or in other words, appears to slip between the mixture bulk and the wall.

Considering that $\hat{\xi} > 0.44$ holds for $\hat{r} < 0.22$ at $\tau = 1.25 \times 10^{-5}$ in the inset of Fig. 10(a), the spatial resolution of our coarse-grained description in this region near the tube axis

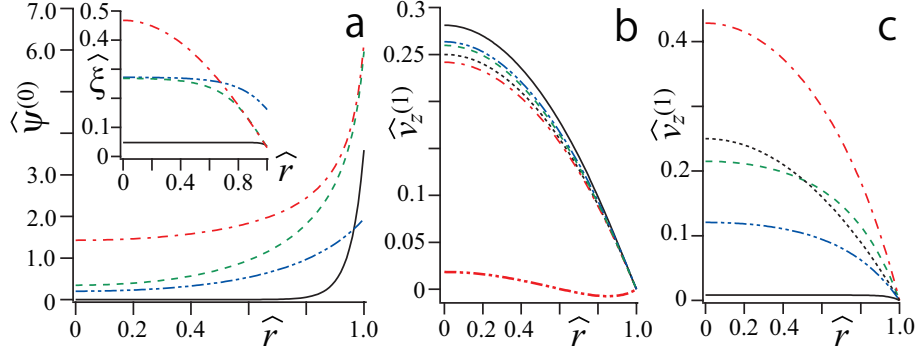


FIG. 10: Calculation results for a mixture of LW. Against \hat{r} , the dimensionless order parameter $\hat{\psi}^{(0)}(\hat{r})$ is plotted in (a), the dimensionless correlation length $\hat{\xi}$ at equilibrium is plotted in the inset of (a), $\hat{v}_z^{(1)}$ for $(\delta\hat{P}, \delta\hat{\mu}) = (-\varepsilon, 0)$ is plotted in (b), and $\hat{v}_z^{(1)}$ for $(\delta\hat{P}, \delta\hat{\mu}) = (0, -\varepsilon)$ is plotted in (c), except for the red thicker dash-dot-dot curve at the bottom in (b) and the black dotted curves in (b) and (c). See the second paragraph of Appendix D for these exceptions and the definition of $\hat{v}_z^{(1)}$. The red dash-dot, green dashed, and black solid curves are obtained for $\tau = 1.25 \times 10^{-5}$, 4.0×10^{-4} , and 6.4×10^{-3} , respectively, under $h = 0.1 \text{ cm}^3/\text{s}^2$. The blue dash-dot-dot curves are obtained for $\tau = 4.0 \times 10^{-4}$ and $h = 0.01 \text{ cm}^3/\text{s}^2$.

is approximately $0.44r_{\text{tube}}$. Each of the variations shown by the curves for $\hat{r} < 0.22$ at $\tau = 1.25 \times 10^{-5}$ in Figs. 10(b) and (c) is much smaller than each of the value at $\hat{r} = 0$, indicating that we can trace each velocity profile well on the spatial resolution mentioned above. Each velocity profile exhibits a more rapid change near the tube wall, which can be traced on the local resolution estimated from $\hat{\xi}$, which is smaller there than in the region near the tube axis. Similar discussions are valid for the other curves in Fig. 10. Thus, our coarse-grained description is valid for the velocity fields examined in this figure.

Suppose that the second term is much smaller than the first term in Eq. (39). Then, $\hat{\omega} \approx \hat{\tau}$ holds and the second term in the parentheses of Eq. (38) is negligible. We further approximate M_- to be $k_B T_c C_1$ to obtain the Gaussian model, which is valid for large τ and small $|h|$. We here consider a simple case, where the Gaussian model is valid, η_s is constant, and r_{tube} is so large that the tube wall can be regarded as a plane. Far from the wall in flow driven by the mass-fraction difference, v_z is given by

$$\frac{\delta\mu}{\eta_s L_{\text{tube}}} \int_0^\infty dX_1 \int_{-\infty}^{X_1} dX \psi^{(0)}(X) \quad (\text{D2})$$

owing to Eq. (28). Here, $\psi^{(0)}$ is regarded as a function of the distance from the tube wall, X . From the equations corresponding with Eq. (D1) and the associated boundary condition we have $\psi^{(0)}(X) = h\xi e^{-X/\xi}/M_- = \xi^2 \psi^{(0)''}(X)$, where ξ is homogeneous [65]. Thus, the apparent slip velocity, given by Eq. (D2), becomes

$$-\xi^2 \psi^{(0)}(0) \frac{\delta\mu}{\eta_s L_{\text{tube}}} \approx -2h\xi\rho_c \frac{\delta c_a}{\eta_s L_{\text{tube}}} \quad (\text{D3})$$

because of $\bar{v}_-^{(\text{ref})} \varphi_c \ll 1$. Using $\xi_0 \tau^{-\nu}$ for the homogeneous value of ξ and substituting the parameter values of the black solid curve in Fig. 10(c) into the LHS above, we find the value of \hat{v}_z corresponding with the apparent slip velocity to be 0.008, which agrees with the value shown by the flat part of the black solid curve. For $\delta c_a = -c_{ac}/10$, $L_{\text{tube}} = 10 \mu\text{m}$, $\tau = 6.4 \times 10^{-3}$ and $h = 0.01 \text{ cm}^3/\text{s}^2$, the RHS of Eq. (D3) is approximately 0.1 and $0.9 \mu\text{m}/\text{s}$ for a mixture of LW and a mixture of NEMP, respectively. They agree with the averages of v_z over tube's cross-section calculated from the values of asterisks on the extreme right in Figs. 8(b) and (d), respectively. In passing, the double integral of Eq. (D2) becomes proportional to $\tau^{\nu-\beta-\gamma}$ if we use the universal profile in the critical regime [39, 68].

Appendix E: Transport coefficients

We first mention the previous studies of the dynamic renormalization group calculation for the bulk of a mixture [69–71]. The ψ^4 model is used as a bare model for an incompressible mixture having vanishing average of ψ . In this mixture, ξ is homogeneously equal to $\xi_0 \tau^{-\nu}$. The interdiffusion coefficient equals Λ divided by the osmotic susceptibility, given by $1/f_-''(0)$, and is found to equal $\lambda^* k_o^{4-z_\psi} \xi^{2-z_\psi}$ in a near-critical mixture. Here, λ^* is a constant determined at the fixed point of the renormalization group flow starting from a bare model having k_o as the cutoff wavenumber; $1/k_o$ is a microscopic length scale. With z_η denoting $z_\psi - d$, where d is the spatial dimensions, the singular part of the viscosity, denoted by η_{sing} , becomes given by $\eta^*(k_o \xi)^{z_\eta}$ as the critical point is approached. Here, η^* is a constant determined at the fixed point and is not η_* defined in the text. Thus, in equilibrium order parameter fluctuations at the critical composition, Λ equals

$$\frac{\lambda^*(k_o \xi)^{4-z_\psi}}{f_-''(0) \xi^2} = \frac{R k_B T_c}{f_-''(0) \xi^{d-2} \eta_{\text{sing}}}, \quad (\text{E1})$$

where $f_-''(0)$ is given by Eq. (40) and R is a universal constant called Kawasaki amplitude. The equality above comes from the definition of this constant. Below, d is put equal to

three, as in the text. From the experimental data of $2\Lambda M_-/\xi^4$ at the critical composition [43, 47], the value of $2\lambda^*k_o^{4-z_\psi}\xi_0^{-z_\psi}$ is $2.5 \times 10^{10} \text{ s}^{-1}$ for a mixture of LW, and $1.23 \times 10^{11} \text{ s}^{-1}$ for a mixture of NEMP. Applying these values for the first equality of Eq. (E1), we obtain $\Lambda_* = 2.19 \times 10^{-9} \text{ kg}\cdot\text{s}/\text{m}^3$ and $2.78 \times 10^{-8} \text{ kg}\cdot\text{s}/\text{m}^3$ for respective mixtures.

The product νz_η is measured to be around 0.042 [44, 45], which leads to $z_\psi = 3.067$. Because of the weak singularity, the viscosity at the critical composition can be well described in the form of multiplicative anomaly as [46, 72]

$$A_\eta \exp \left[\frac{B_\eta}{T - T_\eta} \right] \exp [z_\eta H(\tau, q_D, q_C)] , \quad (\text{E2})$$

where $H(\tau, q_D, q_C)$ is the crossover function with q_D and q_C being wavenumber parameters. It is defined at Eq. (2.18) of Ref. [73], approaches zero as ξ tends to zero, and approaches the sum of $\ln \xi$ and a constant as $q_C \xi$ is larger. Thus, η_{sing} is given by Eq. (E2) with $T - T_\eta$ being replaced by $T_c - T_\eta$. This leads to $\eta_{\text{sing}} \propto \xi^{z_\eta}$ for $T \approx T_c$, as it should do. We approximate η_* to be Eq. (E2) at $T = T_*$, considering that τ_* is very small. The calculation result for Λ in the mode coupling theory [9], agrees with the RHS of Eq. (E1) if R is put equal to $1/(6\pi)$ and if z_η is regarded as zero.

In Eqs. (16) and (17), we need the values of the transport coefficients for off-critical compositions. As in Eq. (4.11) of Ref. [15], we obtain the value of Λ_0 by regarding ξ as given from $\hat{\psi}^{(0)}$ via Eqs. (35) and (39) and replacing $f''(0)$ with $f''(\psi^{(0)})$ in the LHS of Eq. (E1). This definition yields Eq. (42). A similar function for Λ_0 is used in Sec. 4.2 of Ref. [15], where z_ψ is put equal to three. The fraction in the last term in the last entry of Eq. (47) is originally the LHS of Eq. (E3) below. We use the definitions to obtain

$$\frac{2\pi r_{\text{tube}}^2}{L_{\text{tube}}} \times \frac{\Lambda_* T_* \mu_*}{\mathcal{I}_* T \psi_*} = \frac{48 T_c u^* R}{T} . \quad (\text{E3})$$

Approximating T to be T_c and using $R = 1/(6\pi)$, we obtain the fraction in Eq. (47).

We below mention η_s for off-critical compositions. As a fitting function to the data out of the peak in Figs. 2(a) and 5(a), we use

$$A_\eta \exp \left[\frac{B_\eta}{T - T_\eta} \right] + G(c_a - c_{ac}) , \quad (\text{E4})$$

where G is a quartic function vanishing at $c_a = c_{ac}$ [73]. The difference in the parentheses in the second term above represents the variable of G . The dependence of the four coefficients of the quartic function on τ is estimated from curve fitting. Subtracting the background viscosity given by Eq. (E4) from the data, we fit the difference to [74]

$$A_\eta \exp \left[\frac{B_\eta}{T - T_\eta} \right] \{ \exp [z_\eta H(\tau, q_D, q_C)] - 1 \} \exp [-\zeta (c_a - c_{ac})^2], \quad (\text{E5})$$

where ζ is a positive constant to be estimated from the data in the peak. Thus, we can obtain the viscosity as a function of τ and c_a , which can be converted to φ using Eq. (5). The function η_0 is obtained by replacing φ with $\psi^{(0)}(r) + \varphi_c$.

For a mixture of LW at the critical composition immediately below the lower consolute temperature, A_η , B_η , T_η , q_C , and q_D are estimated to be 1.4×10^{-7} Pa · s, 2.916×10^3 K, 0.2 K, 10^{11} m⁻¹, and 10^9 m⁻¹, respectively [47]. Using the experimental data for off-critical compositions in Refs. [48, 49], we find $5.37 + 58.9\tau$, $1.34 + 68.3\tau$, $-13.1 + 71.4\tau$, and $-3.29 - 683\tau$ mPa · s as the coefficients of the linear, quadratic, cubic, and quartic terms of G , respectively. From the data shown by the circles in the peak in Fig. 2(a), we obtain $\zeta = 2.60 \times 10^2$. Equation (E2) with $q_C = 1.3 \times 10^9$ m⁻¹ and $q_D = 3.2 \times 10^8$ m⁻¹ is used for a mixture of NEMP at the critical composition immediately above the upper consolute temperature in Ref. [43]. We use the dashed line in Fig. 1 of this reference as the first term on the RHS of Eq. (E4). The experimental data in Ref. [51] include the values of η_s for off-critical compositions. However, the data at the critical composition are slightly different from those calculated from Eq. (E2) with the values of q_C and q_D mentioned above. Thus, so that they agree with each other, we shift the data for each value of τ in Ref. [51]. The sets of data at $\tau = 1.47 \times 10^{-4}$, 1.82×10^{-3} , and 1.19×10^{-2} are respectively raised by 8.60×10^{-3} , 4.80×10^{-3} , and 1.25×10^{-2} mPa · s. The results are shown in Fig. 5(a). Then, we obtain $0.303 - 2.74\tau$, $-0.812 + 32.8\tau$, $0.212 + 13.5\tau$, and $5.28 - 159\tau$ mPa · s as the coefficients of the linear, quadratic, cubic, and quartic terms of G , respectively, and obtain $\zeta = 2.66 \times 10^2$.

The life time of a correlated cluster with the size of ξ in the order-parameter fluctuations would be given by the inverse of $\Lambda f''(0)/\xi^2$. If the inverse of the shear rate of a flow is smaller than the life time, the cluster is deformed and the critical enhancement of the transport coefficients Λ and η_s is suppressed [71, 75–77]. Using the RHS of Eq. (E1) and

taking the shear to be U/r_{tube} , where U is defined in the penultimate paragraph of Section VI, we find that the suppression does not occur when U is smaller than approximately $100 \mu\text{m/s}$ for $r_{\text{tube}} = 0.1 \mu\text{m}$, $\xi = 50 \text{ nm}$ and $\eta_s = 2 \text{ mPa}\cdot\text{s}$. In the presence of PA, ξ being much smaller near the tube wall, the Onsager coefficients are little affected by the critical enhancement and hence by its suppression, as far as examined in the present study.

-
- [1] J. W. Cahn, "Critical point wetting," J. Chem. Phys. **66**, 3667 (1977).
 - [2] D. Beysens and D. Estève, "Adsorption phenomena at the surface of silica spheres in a binary liquid mixture," Phys. Rev. Lett. **54**, 2123 (1985).
 - [3] D. Beysens and S. Leibler, "Observation of an anomalous adsorption in a critical binary mixture," J. Physique Lett. **43**, 133–136 (1982).
 - [4] D. Bonn and D. Ross, "Wetting transitions," Rep. Prog. Phys. **64** 1085–1163 (2001).
 - [5] M. N. Binder, *Phase Transitions and Critical Phenomena VIIIIV*, Critical behavior at surfaces. (Academic, London, 1983).
 - [6] R. Okamoto, Y. Fujitani, and S. Komura, "Drag coefficient of a rigid spherical particle in a near-critical binary fluid mixture," J. Phys. Soc. Jpn **82**, 084003 (2013).
 - [7] A. Furukawa, A. Gambassi, S. Dietrich, and H. Tanaka, "Nonequilibrium critical Casimir effect in binary fluids," Phys. Rev. Lett. **111**, 055701 (2013).
 - [8] A. Onuki, *Phase Transition Dynamics* (Cambridge University Press, 2002), Chapter 6.1.2.
 - [9] K. Kawasaki, "Kinetic equations and time correlation functions of critical fluctuations," Ann. Phys. (N.Y.) **61**, 1 (1970)
 - [10] T. Ohta, "Selfconsistent calculation of dynamic critical exponents for classical liquid," Prog. Theor. Phys. **54**, 1566 (1975).
 - [11] M. E. Fisher, and H. Au-Yang, "Critical wall perturbations and a local free energy functional," Physica A **101**, 255 (1980).
 - [12] R. Okamoto and A. Onuki, "Casimir amplitude and capillary condensation of near-critical binary fluids between parallel plates: Renormalized local functional theory," J. Chem. Phys. **136**, 114704 (2012).
 - [13] Y. Fujitani, "Undulation amplitude of a fluid membrane in a near-critical binary fluid mixture calculated beyond the Gaussian model supposing weak preferential attraction," J.

- Phys. Soc. Jpn. **86** 044602 (2017).
- [14] S. Yabunaka, R. Okamoto, and A. Onuki, "Hydrodynamics in bridging and aggregation of two colloidal particles in a near-critical binary mixture," *Soft Matter* **11**, 5738 (2015).
- [15] S. Yabunaka and Y. Fujitani, "Drag coefficient of a rigid spherical particle in a near-critical binary fluid mixture, beyond the regime of the Gaussian model," *J. Fluid Mech.* **886** A2 (2020).
- [16] S. R. de Groot and G. Mazur, *Non-equilibrium thermodynamics*, (Dover, New York, 1984). Section IV and Chapter XV.
- [17] S. Samin and R. van Roij, "Interplay between adsorption and hydrodynamics in nanomechanics: Towards tunable membranes," *Phys. Rev. Lett.* **118**, 014502 (2017).
- [18] P. G. Wolynes, "Osmotic effects near the critical point," *J. Phys. Chem.* **80**, 1570–1572 (1976).
- [19] X. Xu and T. Qian, "Generalized Lorentz reciprocal theorem in complex fluids and in non-isothermal systems," *J. Phys.: Condens. Matter* **31**, 475101 (2019).
- [20] Y. Uematsu and T. Araki, "Electro-osmotic flow of semidilute polyelectrolyte solutions," *J. Chem. Phys.* **139**, 094901 (2013).
- [21] C. Lee, C. Cottin-Bizonne, A.-L. Biance, P. Joseph, L. Bocquet, and C. Ybert, "Osmotic flow through fully permeable nanochannels," *Phys. Rev. Lett.* **112**, 244501 (2014).
- [22] H. J. Keh, "Diffusiophoresis of charged particles and diffusioosmosis of electrolyte solutions," *Curr. Opin. Coll. Interf. Sci.* **24**, 13–22 (2016).
- [23] M. Atlas, Rizwan Ul Haq, and T. Mekkaoui, "Active and zero flux of nanoparticles between a squeezing channel with thermal radiation effects," *J. Mol. Liq.* **223**, 289 (2016).
- [24] D. Velegol, A. Garg, R. Gusha, A. Kar, and M. Kumar, "Origins of concentration gradients for diffusiophoresis," *Soft Matter* **12**, 4686 (2016).
- [25] M. Hamid, M. Usman, Z.H. Khan, R. U. Haq, and W. Wang, "Numerical study of unsteady MHD flow of Williamson nanofluid in a permeable channel with heat source/sink and thermal radiation," *Eur. Phys. J. Plus* **133**, 527 (2018).
- [26] S. Marbach and L. Bocquet, "Osmosis, from molecular insights to large-scale applications," *Chem. Soc. Rev.* **48**, 3102–3144 (2019).
- [27] S. Shin, "Diffusiophoretic separation of colloids in microfluidic flows," *Phys. Fluids* **32**, 101302 (2020).
- [28] B. L. Werkhoven and R. van Roij, "Coupled water, charge and salt transport in heterogeneous

- nano-fluidic systems,” *Soft Matter* **16**, 1527–1537 (2020).
- [29] V. S. Sivasankar, S. A. Etha, H. S. Sachar, and S. Das, “Ionic diffusioosmotic transport in nanochannels grafted with pH-responsive polyelectrolyte brushes modeled using augmented strong stretching theory,” *Phys. Fluids* **32**, 042003 (2020).
- [30] S. Ramírez-Hinestrosa and D. Frenkel, “Challenges in modelling diffusiophoretic transport,” *Eur. Phys. J. B* **94**, 199 (2021).
- [31] C. Sun, R. Zhou, Z. Zhao, and B. Bai, “Extending the classical continuum theory to describe water flow through two-dimensional nanopores,” *Langmuir* **37**, 6158–6167 (2021).
- [32] B. V. Derjaguin, S. S. Dukhin, and V. V. Koptelova, “Capillary osmosis through porous partitions and properties of boundary layers of solutions,” *J. Coll. Interf. Sci.* **38**, 584–595 (1972).
- [33] J. L. Anderson, “Colloid transport by interfacial forces,” *Ann. Rev. Fluid Mech.* **21**, 61–99 (1989).
- [34] Y. Fujitani, “Diffusiophoresis in a near-critical binary fluid mixture,” *Phys. Fluids* **34**, 041701 (2022).
- [35] L. Onsager, “Reciprocal relations in irreversible processes I,” *Phys. Rev.* **37**, 405 (1931).
- [36] L. Onsager, “Reciprocal relations in irreversible processes II,” *Phys. Rev.* **37**, 2265 (1931).
- [37] A. J. Bray and M. A. Moore, “Critical behaviour of semi-infinite systems,” *J. Phys. A: Math. Gen.* **10**, 1927–1962 (1977).
- [38] H. W. Diehl, *Phase Transition and Critical Phenomena X*, Field theoretical approach to critical behavior at surfaces. (Academic, London, 1986).
- [39] H. W. Diehl, “The theory of boundary critical phenomena,” *Int. J. Mod. Phys. B* **11**, 3503–3523 (1997).
- [40] R. Okamoto and A. Onuki, “Attractive interaction and bridging transition between neutral colloidal particles due to preferential adsorption in a near-critical binary mixture,” *Phys. Rev. E* **88**, 022309 (2013).
- [41] S. Yabunaka and A. Onuki, “Critical adsorption profiles around a sphere and a cylinder in a fluid at criticality: Local functional theory,” *Phys. Rev. E* **96**, 032127 (2017).
- [42] A. Pelissetto and E. Vicari, “Critical phenomena and renormalization-group theory,” *Phys. Rep.* **368**, 549 (2002).
- [43] I. Iwanowski, K. Leluk, M. Rudowski, and U. Kaatzke, “Critical dynamics of the binary system

- nitroethane/3-methylpentane: Relaxation rate and scaling function,” *J. Phys. Chem. A* **110**, 4313 (2006).
- [44] R. F. Berg and M. R. Moldover, ”Critical exponent for the viscosity of four binary liquids,” *J. Chem. Phys.* **89**, 3694–3704 (1989).
- [45] R. F. Berg and M. R. Moldover, ”Critical exponent for viscosity,” *Phys. Rev. A* **42**, 7183–7187 (1990).
- [46] J. V. Sengers, ”Transport properties near critical points,” *Int. J. Thermophys.* **6**, 203–232 (1985).
- [47] S. Z. Mirzaev, R. Behrends, T. Heimburg, J. Haller, and U. Kaatzke, ”Critical behavior of 2,6-dimethylpyridine-water: Measurements of specific heat, dynamic light scattering, and shear viscosity,” *J. Chem. Phys.* **124** 144517 (2006).
- [48] A. Stein, S. J. Davidson, J. C. Allegra, and G. F. Allen, ”Tracer Diffusion and Shear Viscosity for the System 2,6-Lutidine-Water near the Lower Critical Point,” *J. Chem. Phys.* **56** 6164 (1972).
- [49] C. A. Grattoni, R. A. Dawe, C. Y. Seah, and J. D. Gray, ”Lower Critical Solution Coexistence Curve and Physical Properties (Density, Viscosity, Surface Tension, and Interfacial Tension) of 2,6-Lutidine + Water,” *Chem. Eng. Data*, **38**, 516–519 (1993).
- [50] Y. Jayalakshmi, J. S. Van Duijneveldt, and D. Beysens, ”Behavior of density and refractive index in mixtures of 2,6-lutidine and water,” *J. Chem. Phys.* **100** 604–609 (1994).
- [51] H. M. Leister, J. C. Allegra, and G. F. Allen, ”Tracer diffusion and shear viscosity in the liquid-liquid critical region,” *J. Chem. Phys.* **51** 3701 (1969).
- [52] J. Reeder, T. E. Block, and C. M. Knobler, ”Excess volumes of nitroethane + 3-methylpentane,” *J. Chem. Thermodyn.* **8**, 133 (1976).
- [53] H. L. Swinney and D. L. Henry, ”Dynamics of Fluids near the Critical Point: Decay Rate of Order-Parameter Fluctuations,” *Phys. Rev. A*, **8**, 2586–2617 (1973).
- [54] N. Sharifi-Mood, J. Koplik, and C. Maldarelli, ”Molecular Dynamics Simulation of the Motion of Colloidal Nanoparticles in a Solute Concentration Gradient and a Comparison to the Continuum Limit,” *Phys. Rev. Lett.* **111**, 184501 (2013).
- [55] K. Miyazaki, D. Bedeaux, and K. Kitahara, ”Nonequilibrium thermodynamics of multicomponent systems,” *Physica A* **230**, 600 (1996).
- [56] C. W. Gardiner, *Handbook of Stochastic Methods*, (Springer, Berlin, 1985). Section 5.3.

- [57] S. Yabunaka, R. Okamoto, and A. Onuki, "Phase separation in a binary mixture confined between symmetric parallel plates: capillary condensation transition near the bulk critical point", *Phys. Rev. E* **87**, 032405 (2013).
- [58] Y. Tsori and L. Leibler, "Phase-separation in ion-containing mixtures in electric fields", *Proc. Nat. Acad. Sci.* **104**, 7348–7350 (2007).
- [59] S. Samin and Y. Tsori, "Attraction between like-charge surfaces in polar mixtures", *Europhys. Lett.* **95** 36002 (2011).
- [60] S. Samin and Y. Tsori, "Reversible pore-gating in aqueous mixtures via external potential", *Coll. Interf. Sci. Comm*, **12**, 9 (2016)
- [61] R. Okamoto and A. Onuki, "Precipitation in aqueous mixtures with addition of a strongly hydrophilic or hydrophobic solute", *Phys. Rev. E* **82**, 051501 (2010).
- [62] R. Okamoto and A. Onuki, "Charged colloids in an aqueous mixture with a salt", *Phys. Rev. E* **84**, 051401 (2011).
- [63] H. W. Diehl and H. K. Janssen, "Boundary conditions for field theory of dynamic critical behavior in semi-infinite systems with conserved order parameter," *Phys. Rev. A* **45**, 7145 (1992).
- [64] Y. Fujitani, "Effective viscosity of a near-critical binary fluid mixture with colloidal particles dispersed dilutely under weak shear," *J. Phys. Soc. Jpn.* **83**, 084401 (2014).
- [65] Y. Fujitani, "Relaxation rate of the shape fluctuation of a fluid membrane immersed in a near-critical binary fluid mixture," *Eur. Phys. J. E* **39** 31 (2016).
- [66] K. To, "Coexistence curve exponent of a binary mixture with a high molecular weight polymer," *Phys. Rev. E.* **63**, 026108 (2001).
- [67] A. M. Wims, D. McIntyre, and F. Hynne, "Coexistence curve for 3-methylpentane-nitroethane near the critical point," *J. Chem. Phys.* **50** 616 (1969).
- [68] M. E. Fisher and P. G. de Gennes, "Phénomènes aux parois dans un mélange binaire critique," *C. R. Acad. Sci. Paris B* **287**, 207 (1978).
- [69] E. D. Siggia, P. C. Hohenberg, and B. I. Halperin, "Renormalization-group treatment of the critical dynamics of the binary-fluid and gas-liquid transitions," *Phys. Rev. B* **13**, 2110–2123 (1976).
- [70] R. Folk and G. Moser, "Critical dynamics: a field-theoretical approach," *J. Phys. A: Math. Gen.* **39**, R207–R313 (2006).

- [71] A. Onuki and K. Kawasaki, "Nonequilibrium steady state of critical fluids under shear flow: a renormalization group approach," *Ann. Phys. (N.Y.)* **121**, 456–528 (1979).
- [72] T. Ohta, "Multiplicative renormalization of the anomalous shear viscosity in classical liquids," *J. Phys. C: Solid State Phys.* **10**, 791 (1977).
- [73] J. K. Bhattacharjee, R. A. Ferrell, R. S. Basu, and J. V. Sengers, "Crossover function for the critical viscosity of a classical fluid," *Phys. Rev. A*, **24**, 1469 (1981).
- [74] B. C. Tsai and D. McIntyre, "Shear viscosity of nitroethane-3-methylpentane in the critical region," *J. Chem. Phys.* **60**, 937 (1974).
- [75] A. Onuki, "Phase transitions of fluids in shear flow," *J. Phys, Condensed Matter* **9**, 6119–6157 (1997).
- [76] D. Beysens, "Brownian motion in strongly fluctuating liquid," *Thermodynamics of Interfaces and Fluid Mechanics* **3**, 1–8 (2019).
- [77] Y. Fujitani, "Suppression of viscosity enhancement around a Brownian particle in a near-critical binary fluid mixture," *J. Fluid Mech.* **907**, A21 (2021).